

Effects of Cross-sectional Shape on the Low Observability of Double Serpentine Nozzles

Seok Hee Ryu^{a,b}, Seong Jin Jo^a, Rho Shin Myong^{a,*}

^aSchool of Mechanical and Aerospace Engineering and Aerospace Systems Research Center,
Gyeongsang National University, 501 Jinjudaero, Jinju, Gyeongnam 52828, South Korea

^bDefense Agency for Technology and Quality, Quality Planning Department, 420 Dongjinro, Jinju,
Gyeongnam 52851, South Korea

*Corresponding author: E-mail address myong@gnu.ac.kr (R.S. Myong)

Abstract

When unmanned combat aerial vehicles (UCAVs) egress from the battlefield after attacking the target, the defensive radar systems detect signals reflected by the cavity structure of the nozzle and engine of the UCAVs, threatening their survivability. Infrared (IR) guided missiles can also threaten them by detecting the gaseous plume and hot engine parts. We present a comprehensive investigation of the effects of the cross-sectional shape of double serpentine nozzles on thrust, IR signature, and radar cross section (RCS), which are associated with propulsive performance and low observability. The fillet radius and cross-sectional shape of the nozzles were considered as the main design variables. The thermal flow field was analyzed using the compressible Navier-Stokes equations, while the IR signature was analyzed with the radiative heat transfer equation with a narrow band model. The RCS was calculated using a multi-level fast multipole method of full Maxwell's equations instead of the approximate methods often employed. The double serpentine (DS) nozzle with an elliptical cross-section showed high pressure recovery and a 9.66% lower IR signature than the DS nozzle with a rectangular cross section. The maximum RCS and mean RCS were lowest for the DS nozzle with an elliptical cross section, with a maximum difference in maximum RCS of 383% and mean RCS of 90% compared with the DS nozzle with a rectangular cross section. The DS nozzle with an elliptical cross section distributes the current more evenly across the central part of the engine than the DS nozzle with a rectangular cross section. The DS nozzle with an elliptical cross-section showed excellent nozzle performance with a negligible difference in thrust. In addition, the results show that the cross-sectional shape of the nozzles has different levels of impact on thrust and pressure recovery (negligible), IR signature (limited), and RCS (significant).

Keywords: Unmanned combat aerial vehicle (UCAV); double serpentine nozzle; cross-sectional shape; infrared signature (IR); radar cross section (RCS)

1. Introduction

Unmanned combat aerial vehicles (UCAVs) have many advantages over manned combat aerial vehicles, especially in that they do not need flight crews onboard. UCAVs eliminate the need for onboard flight crews and can undertake dull, dirty, and dangerous missions [1]. UCAVs are being developed to suppress enemy air defense systems [2]. After performing a mission and attacking a target, the UCAVs need to egress the battlefield [3]. It must be designed and operated to minimize the effectiveness of enemy weapons to an acceptable level [4]. While egressing the battlefield, as shown in Fig. 1, the UCAV is exposed to severe threats from enemy radar and infrared (IR) guided missiles from the rear.

Aircraft IR tracking primarily utilizes mid-wave infrared (MWIR, 3 to 5 μm) and long-wave infrared (LWIR, 8 to 12 μm) bands [5]. Passively guided IR missiles pose a significant threat to aircraft [6]. Advancements in IR seeker technology have profoundly transformed air combat, making careful management of aircraft IR signatures essential for enhancing survivability [7]. Signature suppression aims to reduce the detection and tracking range of IR missiles [8]. The aircraft's IR signature is most pronounced in specific wavelength bands, particularly 8 to 12 μm [9]. The main IR signature source of the rear fuselage is in the 8 to 12 μm band, while the aircraft plume's significance is in the 4.15 to 4.20 μm band due to atmospheric transmittance [10].

Radar has a variety of frequency bands and can detect flying vehicles even at hundreds of kilometers. RCS is measured as the ratio of electromagnetic waves transmitted from radar that bounce back after hitting an object, and the aircraft's size, shape, material, and structure influence the RCS. The engine intakes and nozzles are among the most important elements in RCS [11]. Multiple reflections and scattering can occur inside the engine nozzle, which has an open-ended cavity structure, significantly affecting the RCS [12].

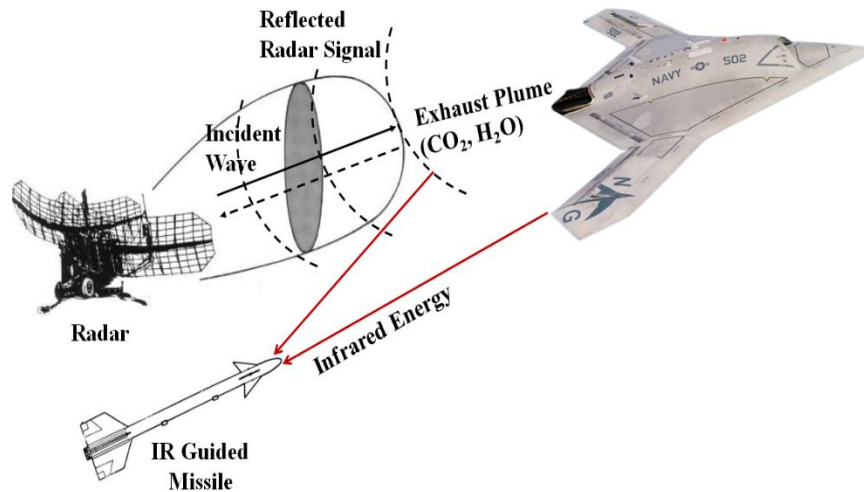


Fig. 1. Schematic of UCAV survivability when threatened by radar/IR guided missiles.

UCAVs are equipped with serpentine nozzles to make them less observable and enhance their survivability. The serpentine nozzle significantly reduces its IR signature by shielding the high-temperature parts of the engine, which are the primary source of the IR signature [13]. On the other hand, when the nozzle is exposed to radar, the curvature of the serpentine nozzle generates different RCS characteristics than a conventional asymmetric nozzle [14]. To assess the survivability of UCAVs in detail, it is necessary to analyze the flowfield and associated electromagnetic fields of the serpentine nozzle, and in particular, their spectral characteristics in radio and IR frequencies.

As summarized in Table 1, several groups have studied the low-observable characteristics of serpentine nozzles in the past. Baranwal et al. [15] analyzed how reducing the circular nozzle exit area blocks hot parts, but the resulting increase in back pressure ultimately raises the IR signature. Baranwal et al. [16] also analyzed the impact on hot part visibility and IR radiance in the 1.9–2.9 μm and 3–5 μm bands. X. Sun et al. [17] analyzed the internal flow of a double serpentine nozzle with different center line curvatures using experiments and computational fluid dynamics (CFD) based on Reynolds-averaged Navier-Stokes (RANS) equations. When designing the double serpentine nozzle, the optimal ratio of the double curvature length was suggested to be 2:5 to 2:3. P. Sun et al. [18] analyzed the internal flow characteristics of the serpentine nozzle for varying bypass ratios. Cheng et al. [13] analyzed the change in IR radiation intensity according to differences in the shielding ratio of single/double serpentine nozzles.

The IR signature of the serpentine nozzle was 28.9% lower compared to a conventional circular nozzle. An appropriate shield ratio for the single/double serpentine nozzles was also suggested. Lindermeir et al. [19] analyzed the plume temperature and IR signature of a UCAV equipped with a double serpentine nozzle. Considering the atmospheric environment and plume, a high IR signature was confirmed when observed against the sky background. Shan et al. [20] analyzed how the IR signature was affected by the offset ratio, the ratio of length to diameter, and the aspect ratio of a double serpentine nozzle. When the offset ratio was 0.25, the pressure recovery and thrust coefficients increased by 6.3% and 11.7%, respectively. The IR signature was shown to be reduced by the aspect ratio by more than 50%. Cheng et al. [21] investigated the effect of engine swirl on the IR signature of the serpentine nozzle. They determined engine swirl could effectively suppress the IR signature, and the total IR signature level decreased by 13.84% in the horizontal plane and 31.21% in the vertical plane. Noh et al. [22] analyzed flow characteristics and IR signature after installing a serpentine nozzle inside a UCAV and confirmed that the double serpentine nozzle reduced the IR signature by 22.4%. Hui et al. [23] investigated the flow and thrust characteristics of the serpentine and axisymmetric nozzles with experiments. Meng et al. [24] analyzed the effects of the serpentine configuration and nozzle pressure ratio on the flow characteristics of a multi-stream supersonic nozzle, demonstrating maximum thrust performance with a nozzle pressure ratio of 7.0.

Radar is one of the most effective ways of detecting flying objects at ranges of hundreds of kilometers. Table 2 shows the threat types and radar frequency bands that affect aircraft survivability. Most radars operate in the X- and Ku-bands because these provide precise target locations with less power and a much smaller package. Low-observable UCAVs should thus be designed to improve low-observability for C-, X-, and Ku-bands [25].

Currently, research is being actively conducted to investigate the effect of the serpentine nozzle on RCS characteristics. Brown [28] confirmed that the multiple reflections of an S-duct-shaped cavity structure had more bounces than a cylindrical one. He et al. [12] determined the optimal design shape of the serpentine nozzle for RCS reduction. They demonstrated an RCS reduction of up to 90.39% compared to the original nozzle. In addition, the backscatter from the nozzle shape was investigated by analyzing the induced current on the nozzle wall according to the detected angle. Guo et al. [29] measured the RCS

of a double serpentine nozzle with and without radar-absorbing material (RAM). Zhou and Huang analyzed the IR and RCS characteristics of advanced fighter intake and exhaust systems using a comprehensive design method [30] and a mixed design approach [31]. He et al. [32] investigated the thrust and electromagnetic characteristics of an S-shaped inlet with an internal bump based on curvature control. The higher shielding ratio nozzle improved electromagnetic performance and decreased the electromagnetic objective function by 70.33%.

Table 1 Literature review of previous studies on low-observability of the nozzle.

Authors (Year)	Nozzle Parameters	Flowfield	IR Signature	RCS	Flight Condition
Cheng et al. (2017) [15]	Shield Ratio	RANS	Discrete Transfer Method	-	Ground
Guo et al. (2017) [29]	RAM	-	-	Experiment	-
Sun et al. (2018) [18]	Bypass Ratio	RANS	-	-	Ground
Lindermeir et al. (2018) [19]	Split Nozzle	RANS	Bidirectional Path Tracing	-	Cruise
Shan et al. (2019) [20]	Offset Ratio, Aspect Ratio	Experiment, RANS	Forward-Backward Ray Tracing Method	-	Ground
Zhou and Huang (2021) [31]	Nozzle Shape	RANS	Ray Tracing Method	PO and Physical Theory of Diffraction	Ground
He et al. (2022) [32]	Cross-sectional Shape	RANS	-	Forward-Backward Iterative Physical Optics (PO)	Cruise

Meng et al. (2023) [24]	Centerline, Cross-sectional Shape	RANS	-	-	Ground
Present	Cross-sectional Shape	RANS	Narrow Band Model	Multilevel Fast Multipole Method (MLFMM) of Full Maxwell's Equations	Cruise

Table 2 Radar threats type and radar band [26, 27].

Radar system	Band	Frequency [GHz]	Wavelength [in]
Early Warning	VHF	0.15-0.2	70-80
	S	3-4	3-4
Ground-control Intercept	S	2-3	3-5
Height Finders	S	2-7	1-5
	C		
Airborne Early Warning			
Aircraft	UHF	0.3-1	12-40
	S	2-4	3-6
	X, Ku	8-18	0.6-1.5
AAM	X	9	1
SAM Strategic			
Acquisition	VHF, L, S	0.15-3	3-70
Tracking	C, X, Ku	5-13	0.9-2.4
SAM tactical			
Acquisition	S, C	2-6	2-5
Tracking	C, X	5-13	1-2
Radar-guided AAA	Ku	14-16	0.6-0.7

* AAM: Air-to-Air Missile

* SAM: Surface-to-Air Missile

* AAA: Anti-Aircraft Artillery

An et al. [33] investigated the thrust and IR characteristics of a single serpentine nozzle with varying aspect ratios and curvatures. While the aspect ratio and curvature each reduced the plume temperature, the aspect ratio was found to be more dominant. Compared to a circular nozzle, a high aspect ratio nozzle reduced the IR lock-on range by 55%. Kang et al. [34] designed single serpentine nozzles with different curvature functions, area functions, and aspect ratios, and performed an optimization study with IR

signature level as the objective function. As a result, they presented a single serpentine nozzle configuration with a maximum 83.6% reduction in IR signature without thrust loss. Lee et al. [35] considered double serpentine nozzles with different cross-sectional shapes and investigated thrust and IR characteristics. They reported a double serpentine nozzle configuration with up to 91.5% and 87% reduction in plume and solid wall IR levels, respectively, with a negligible thrust penalty of 0.7%.

To further improve the low observability of UCAVs, research on serpentine nozzles is being actively pursued from various approaches. *However, to the best of the authors' knowledge, there are no previous studies that consider all three characteristics of the double serpentine nozzle; the thrust (including nozzle pressure recovery), IR, and RCS. Additionally, most previous studies have used approximate methods, such as physical optics (PO), and few studies have used the high-fidelity methods of the full Maxwell equations for RCS calculations.*

To fill these gaps, in this study, we investigate the effects of the cross-sectional shape on thrust and low observability, which are associated with the IR and RCS signatures of double serpentine nozzles. The fillet radius and cross-sectional shape of the nozzles are considered as the design variable. A nozzle with an elliptic cross-sectional shape, and rectangular nozzles with fillet radius of 60, 30, and 2 mm, are considered. The thermal flow field inside and outside the nozzle is analyzed with the compressible Reynolds-averaged Navier-Stokes equations. The IR signature is analyzed with the radiative heat transfer equation with a narrow band model. The RCS is calculated using a multi-level fast multipole method of full Maxwell's equations.

2. Design of a double serpentine nozzle

This study considers a scaled-down model of the RM12 engine, a 12,000 lbf turbofan engine from Volvo Aero. The nozzle inlet diameter (D_i) of this model is 500 mm, and the length (L) is 3.5 times the inlet diameter. The center curve that serves as the standard for the double serpentine (DS) nozzle is shown in Fig. 2. L_0 is a straight section for stabilizing the core and bypass flow from the engine, and L_3 is a straight section for stabilizing the flow after the two center curves. L_1 and L_2 are center curves 1 and 2, and the length ratio of $L_1:L_2$ is about 2:3 [18]. The reference line is the x -direction line at the point where the two center curves are tangential. In the DS nozzles, the height differences between the reference line

and the inlet/outlet of the nozzle are ΔY_1 (100 mm) and ΔY_2 (200 mm). The ΔY_1 and ΔY_2 of the straight nozzle is 0 mm. The shield ratio for the DS nozzles is 0.45, while the straight nozzle is 0.0 [13].

Figure 3 shows the geometry of the DS-Elliptic and DS-Rectangular nozzles. The fillet radius is considered to be the main design variable of the DS-Rectangular nozzle. Table 3 shows five nozzles with different fillet radii: Straight, DS-Elliptic, DS-Rectangular 60, DS-Rectangular 30, and DS-Rectangular 2 nozzles. The maximum value of the fillet radius is 60 mm and the DS-Rectangular 2 nozzle with a 2 mm fillet radius is close to a rectangle shape.

The visible line is the range of the line where the inlet of the nozzle can be observed, and the core of the engine is not observed at the rear ($\theta = 0^\circ$). The straight nozzle has a range from -7.5° to 7.5° , but the DS nozzles range from 7.5° to 12.5° and the high-temperature plume of the engine is not observed at the rear due to shield ratio. Specifically, the DS-Elliptic nozzle ranges from 7.5° to 12.5° , and the DS-Rectangular nozzles range from 7.5° to 10° . When the exit area and aspect ratio are the same, the angle increases because the minor axis of the DS-Elliptic nozzle is 11.4% longer. The aspect ratio is 5, which is defined as the ratio (a/b) of the major axis (a) and minor axis (b) of the nozzle outlet [17].

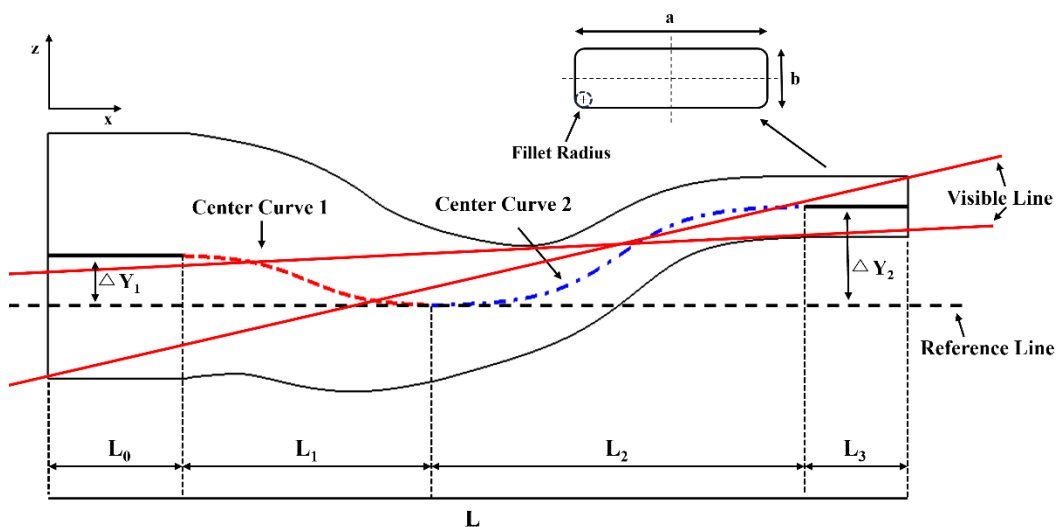


Fig. 2. Schematic of the double serpentine nozzle.

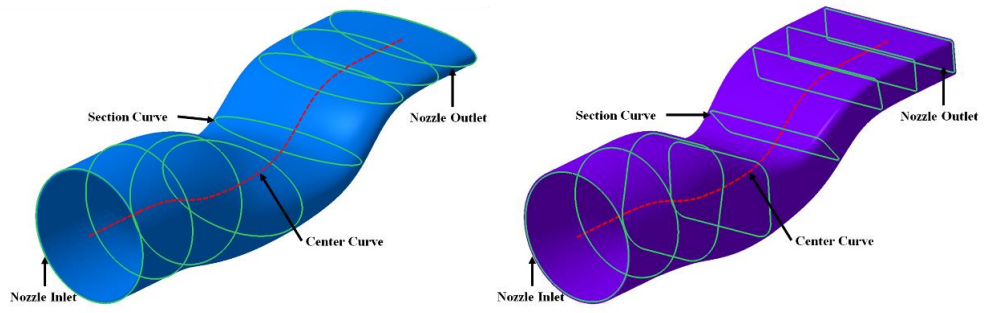
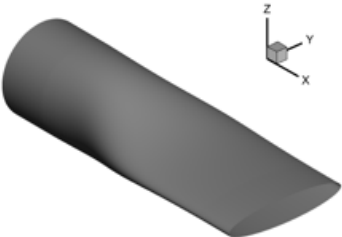
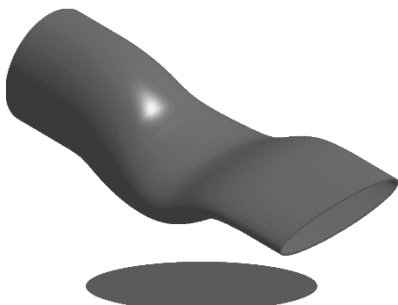
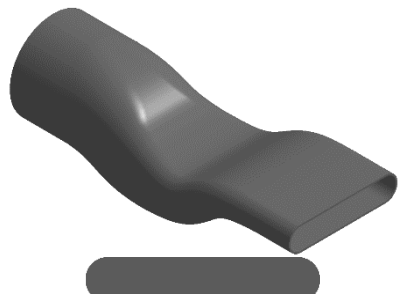
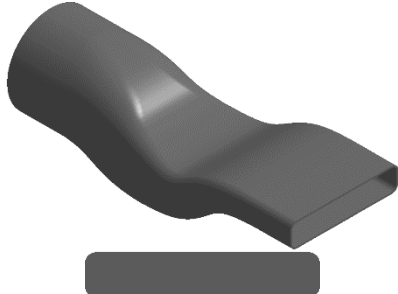
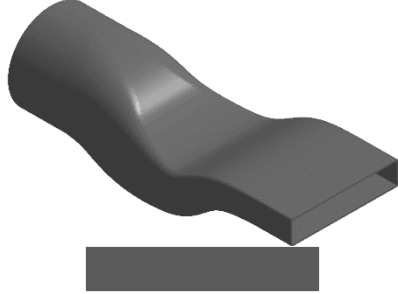


Fig. 3. Geometry of DS-Elliptic and DS-Rectangular nozzles.

Table 3 Geometries and fillet radius of the double serpentine nozzles.

Nozzle	Fillet Radius	Visible Line	Nozzle Shape
Straight	-	7.5° to 7.5°	
DS-Elliptic	-	7.5° to 12.5°	
DS-Rectangular 60	60 mm	7.5° to 10°	
DS-Rectangular 30	30 mm	7.5° to 10°	
DS-Rectangular 2	2 mm	7.5° to 10°	

3. A CFD solver for analyzing the thermal flow field of DS nozzles

3.1. 3D Compressible Navier-Stokes-Fourier equations of the multi-species gaseous plume

The 3D compressible RANS equations are used to compute the thermal flow field of the plume in the DS nozzles. The equations include compressible and viscous effects and calculate a single gaseous phase with multi-species [36].

$$\frac{\partial(\rho Y_i)}{\partial t} + \nabla \cdot (\rho \mathbf{u} Y_i) = -\nabla \cdot \mathbf{J}_i \text{ where } \mathbf{J}_i = -(\rho D_{i,m} + \frac{\mu_t}{Sc_t}) \nabla Y_i - D_{T,i} \frac{\nabla T}{T}, \quad (1)$$

$$\frac{\partial}{\partial t} (\rho \mathbf{u}) + \nabla \cdot (\rho \mathbf{u} \mathbf{u}) + \nabla p = \nabla \cdot (\boldsymbol{\tau} + \boldsymbol{\tau}_t), \quad (2)$$

$$\frac{\partial}{\partial t} (\rho E) + \nabla \cdot (\rho H \mathbf{u}) = \nabla \cdot [(k + k_t) \nabla T] + S_h, \quad (3)$$

where ρ , \mathbf{u} , p , T , E , H are density, velocity, pressure, temperature, total energy density, and total enthalpy, respectively. \mathbf{J}_i and Y_i are the mass flux and mass fraction of each species. $D_{i,m}$ and $D_{T,i}$ are the mass diffusion coefficient for species i in the mixture and the thermal (Soret) diffusion coefficient, respectively. Sc_t is the turbulent Schmidt number and is defined as $\mu_t / \rho D_t$, where μ_t is the turbulent viscosity and D_t is the turbulent diffusivity. $\boldsymbol{\tau}$, k are the viscous shear stress and the thermal conductivity, respectively. The subscript t indicates changes due to turbulence. The source term S_h denotes additional heat transfer.

ANSYS FLUENT, a density-based finite volume method solver for the compressible RANS equations, was used to investigate the thermal flow field of the DS nozzles. The second-order upwind discretization with a least-square cell-based gradient and second-order implicit temporal integration for achieving a steady state convergence were used. Inviscid numerical flux was calculated using Roe's flux-difference splitting scheme, an approximate Riemann solver. A $k-\omega$ SST turbulence model in which a $k-\omega$ model is applied near the wall while a $k-\varepsilon$ model is applied for external flow away from the wall was employed.

3.2. Validation of the CFD solver using a small turbojet engine

To validate the computational model used in the CFD solver, experimental data obtained from a small turbojet engine, AMT's Olympus HP Engine were used [37]. Thermocouples are located 600 mm behind

the center of the nozzle outlet, and 16 thermocouples are installed at 20 mm intervals. The plume temperature distributions of CFD and experimental results are compared in Fig. 4. As the AR increases, the temperature of the plume decreases. As the AR increases, mixing with the air improves, allowing the plume temperature to cool down more quickly. The Single Serpentine nozzle has a narrower cross-sectional area toward the sides of the nozzle exit compared to the AR 5 nozzle. As a result, the core of the plume is more concentrated at the center, leading to a higher temperature distribution. Experimental and CFD results showed similar temperatures for the plume.

An additional validation case was considered using a micro turbofan engine with a bypass. Figure 5 presents the temperature of the plume cross-section at distances of 1 and 3 nozzle inlet diameters (80 mm) from the nozzle exit. At 3 diameters, non-negligible discrepancies between the CFD and experimental results arise probably due to the limitations of CFD in simulating smooth mixing between the core and bypass. Nonetheless, the error margin near the core is within 6%.

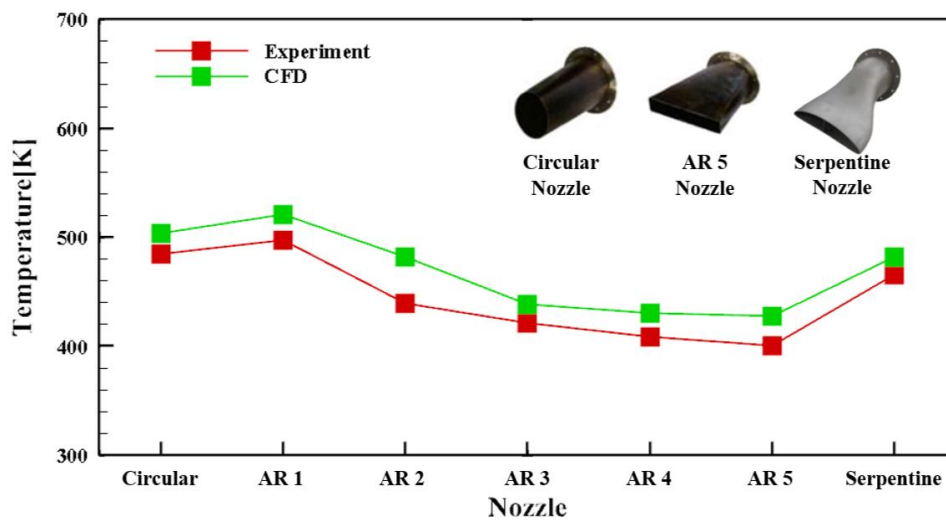


Fig. 4. Validation of CFD models using a micro turbojet engine with various nozzle shapes.

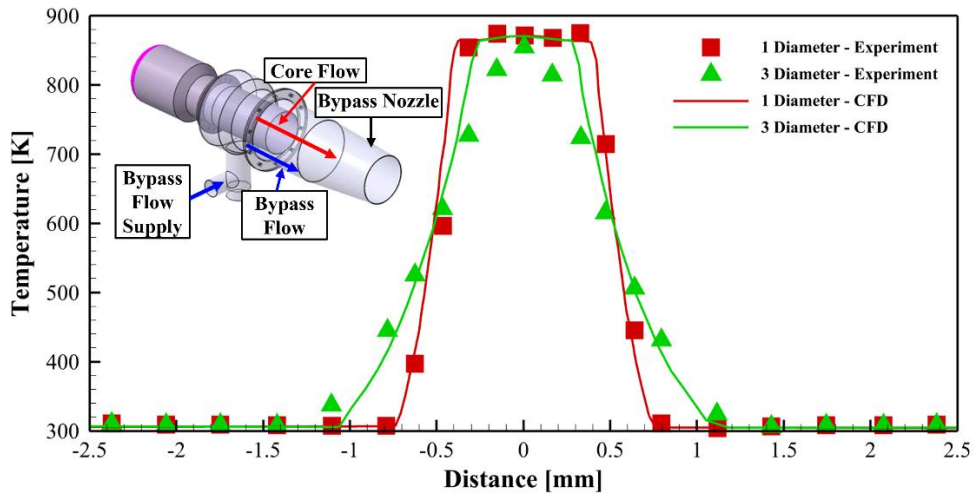


Fig. 5. Validation of CFD models using a micro turbofan engine with a bypass.

3.3. Boundary conditions and computational grids of present DS nozzles

Figure 6 shows the boundary conditions and computational grids of present DS nozzles. The size of the flow field is $30 D_i$ in the circumferential direction and $50 D_i$ in the longitudinal direction. The flow field does not include the external region of the nozzles to prevent the external shape of the nozzle from influencing the plume flow field.

Grid tests were conducted with 3 million, 10 million, and 15 million grids. The 3 million grids predicted a thrust of 7 lbf lower and an exit temperature of 10 K lower than the 10 million grids. The 10 million grids produced results very similar to the 15 million grids. As a result, 10 million polyhedral grids were generated, and more grids were placed inside the nozzle and the plume area.

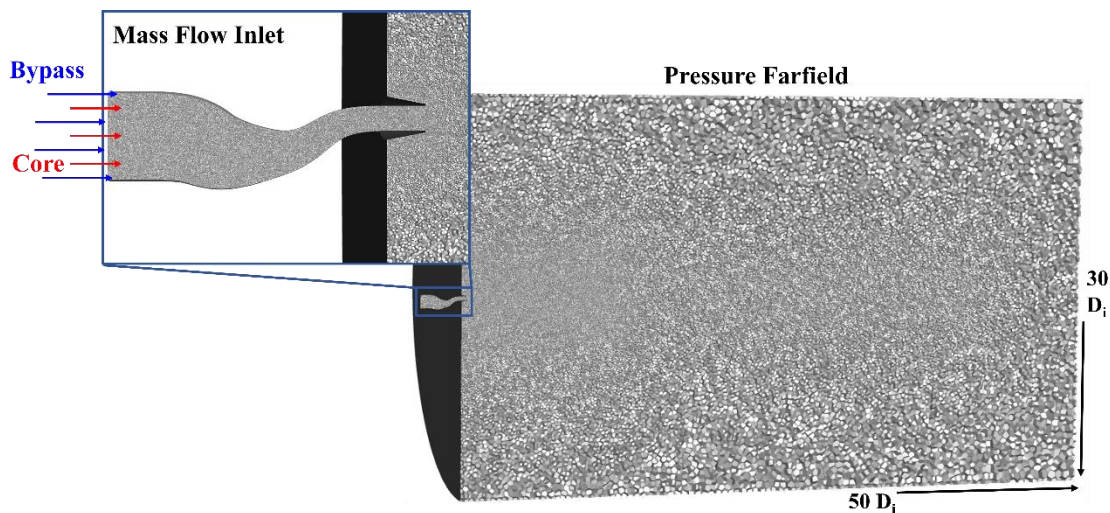


Fig. 6. Boundary conditions and computational grids of the flow field.

A mass flow inlet boundary condition is applied at the nozzle inlet, which includes core and bypass flows. The GASTURB program was used to obtain the engine data needed to set up the nozzle flow. The international standard atmosphere model was used to define the conditions at an altitude of 12km. The cruising condition of Mach number 0.85 was imposed as the pressure far-field, as summarized in Table 4. No-slip and adiabatic conditions were imposed on the nozzle wall. Complete combustion and no additional chemical reactions inside the nozzle were assumed. Multi-species gas flow is assumed to consist of mole fractions of O₂, CO₂, H₂O, and N₂, as summarized in Table 5.

Table 4 Boundary conditions for cruise condition.

Cruise Conditions (Altitude 12km)		
Free-stream (Pressure Far-field)	Pressure (Pa)	19,400
	Temperature (K)	216.7
	Mach Number	0.85
Nozzle Core (Mass Flow Inlet)	Pressure (Pa)	105,579
	Temperature (K)	1,028.24
	Mass Flow Rate (kg/s)	7.784
Nozzle Bypass (Mass Flow Inlet)	Pressure (Pa)	105,576
	Temperature (K)	389.52
	Mass Flow Rate (kg/s)	2.467
Wall	No-slip, Adiabatic	

Table 5 Mole fractions of multi-species gaseous plume flows

	Species	Mole Fraction
Free-stream/ Bypass	N ₂	79%
	O ₂	21%
	CO ₂	-
	H ₂ O	-
Core	N ₂	74%
	O ₂	-
	CO ₂	13%
	H ₂ O	13%

3.4. Propulsive and aerodynamic performance of the DS nozzles

The thrust, a key propulsive performance measure, was found to be up to 1.48% higher for the DS nozzles compared to the Straight nozzle. In the DS nozzles, the variation in thrust with the cross-sectional shape change was within 0.67%. This confirms the cross-sectional shape of the DS nozzles had a negligible effect on the thrust.

Figure 7 shows the pressure recovery and Mach number in the nozzle centerline. Pressure recovery represents the ratio ($P_{t, \text{section}}/P_t$) of the total pressure ($P_{t, \text{section}}$) at the nozzle inner section to the total pressure (P_t) at the nozzle inlet ($x/L = 0$). The closer the pressure recovery is to 1, the lower the pressure loss, meaning better nozzle performance. The pressure recovery of the Straight nozzle ranged from 0.9768 (reduced due to viscous effects) at the inlet to 0.9525 at the nozzle exit. Its value was 0.1 higher than that of the DS nozzles.

When compared with other DS nozzles, the DS-Elliptic nozzle showed the highest pressure recovery. The DS-Rectangular 60, 30, and 2 nozzles exhibited higher pressure recovery. At the nozzle exit ($x/L = 1$), the pressure recovery value for the DS-Elliptic nozzle was 0.9417, and for the DS-Rectangular 60, 30, 2 nozzles it was 0.9363, 0.93504 and 0.9311, respectively. Pressure recovery decreased as the cross-sectional shape of the nozzle exit approached a rectangular shape. Pressure recovery decreased rapidly after x/L was about 0.5. The DS-Rectangular nozzles show a more pronounced decrease in static pressure compared to DS-Elliptic nozzles due to their flat surfaces, which increase the cross-sectional area.

The velocity of the nozzle flow accelerated from Mach number 0.23 to 1.09. The Straight and DS-Elliptic nozzles showed similar Mach number distributions. A slight velocity difference between the DS-Elliptic and DS-Rectangular nozzles occurred in the L_1 and L_2 . Because the cross-sectional shape of the DS-Rectangular nozzle changes more rapidly, the velocity accelerates faster. In L_3 , the velocities of the DS-Elliptic and DS-Rectangular nozzles remained identical. A major dip in the pressure recovery curve occurs after the major rise in the Mach number curves. Both the Mach number and static pressure start to change sharply after $x/L = 0.5$. However, because the increase in dynamic pressure proportional to the square of the Mach number slows the decline in pressure recovery, the main dip in the pressure recovery curve occurs later.

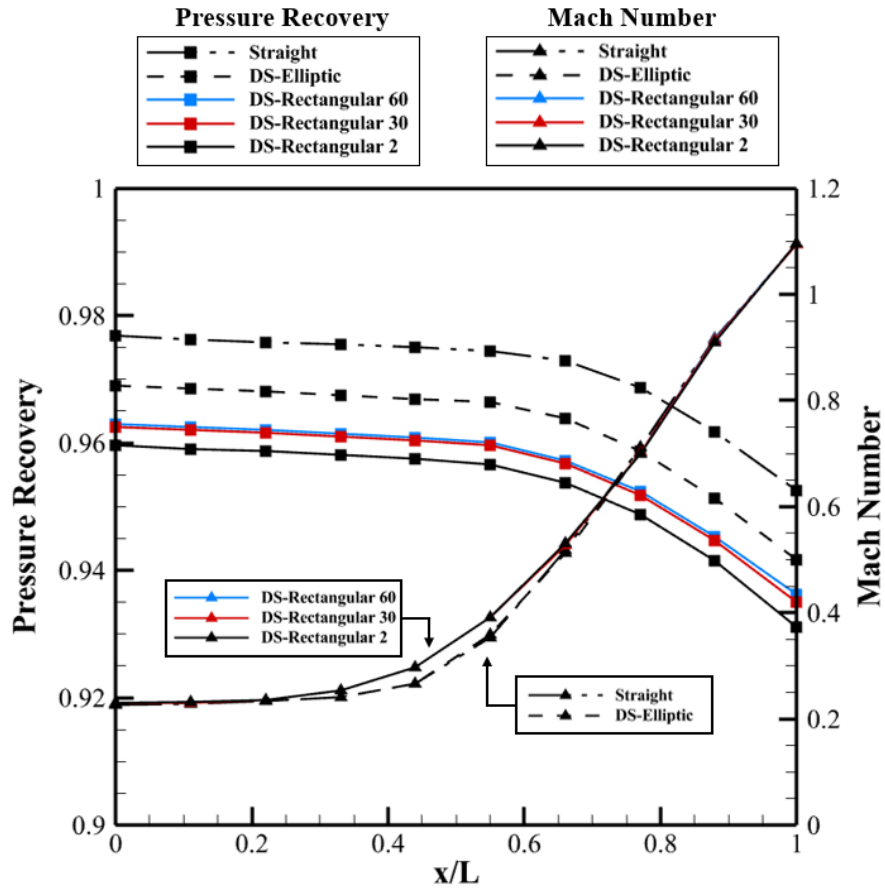


Fig. 7. Pressure recovery and Mach number distribution at the nozzle centerline.

Figure 8 shows the temperature contours of the DS nozzles. After the core flow with a temperature of 1,024 K was mixed with the bypass flow, the average temperature of the plume at the nozzle exit was approximately 754 K. A difference in flow occurs between DS-Elliptic and DS-Rectangular nozzles in the central curved area. The core of the DS-Rectangular nozzle is closer to the upper wall of the nozzle than the DS-Elliptic nozzle. This is because the minor axis radius of the nozzle exit is 11.4% shorter in the DS-Rectangular nozzle. Additionally, the mixing efficiency of the DS-Rectangular nozzle with the core and bypass is lower than that of the DS-Elliptic nozzle. The O_2 mole fraction at the edge is higher in the DS-Rectangular nozzle than in the DS-Elliptic nozzle, which means that the core-bypass mixing is not smooth.

Figure 9 shows the wall temperature contours of the DS nozzles. The nozzle wall temperature increases as the bypass flow contacting the nozzle wall is mixed with the core flow at a higher temperature. The maximum wall temperature of the Straight, DS-Elliptic, DS-Rectangular 60, 30, and 2 nozzles was 859, 856, 882, 884, and 886 K, respectively. The high-temperature wall area was slightly smaller for the DS-Elliptic nozzle than for the DS-Rectangular nozzle.

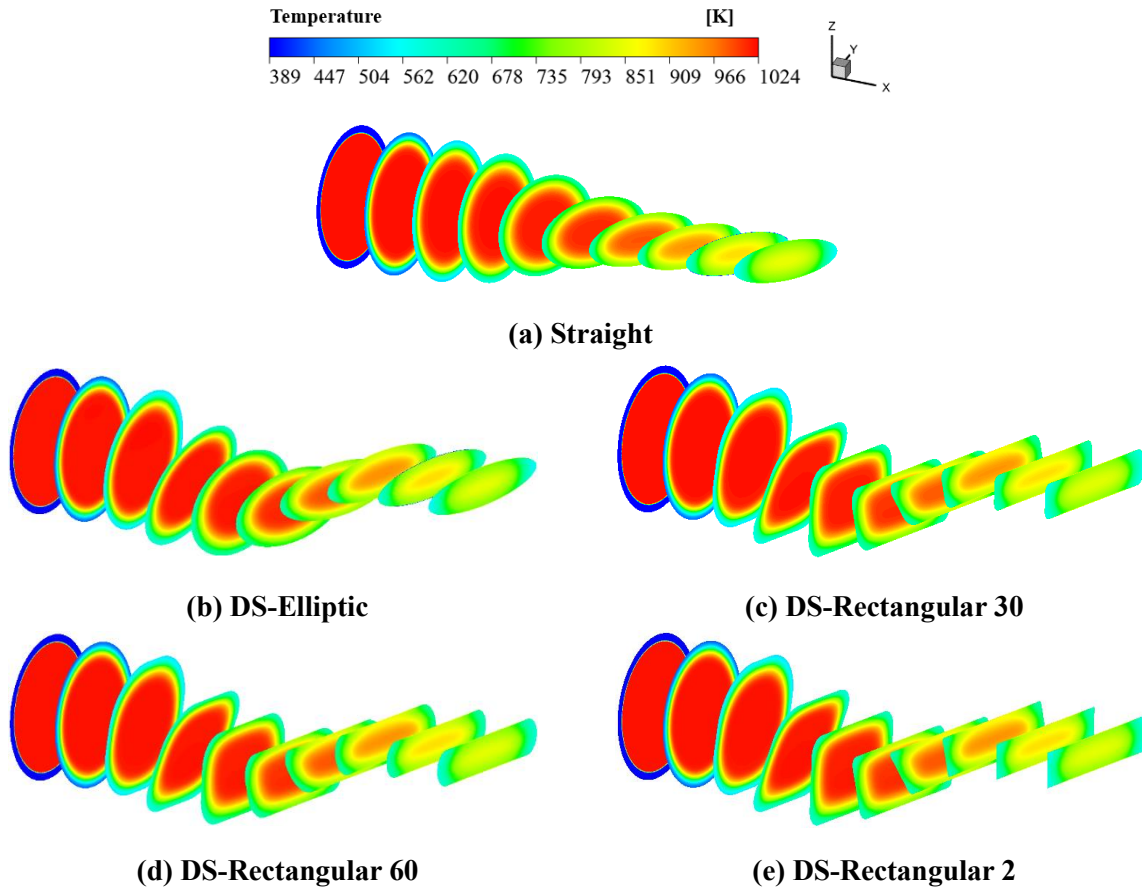
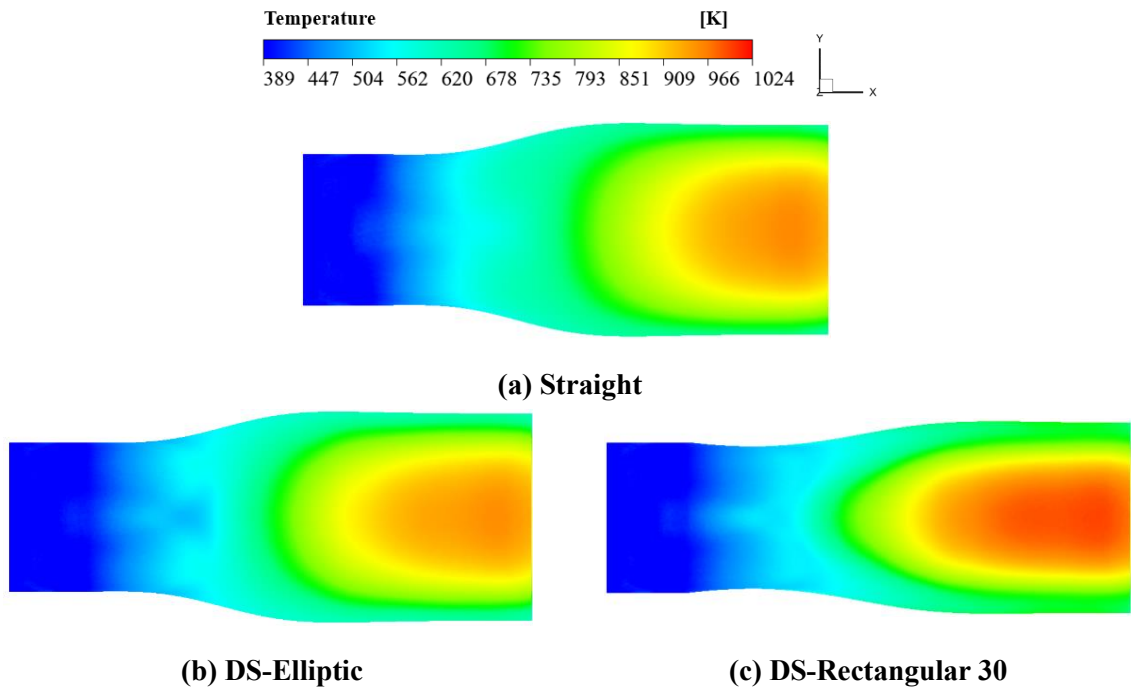


Fig. 8. Temperature contours of the DS nozzles.



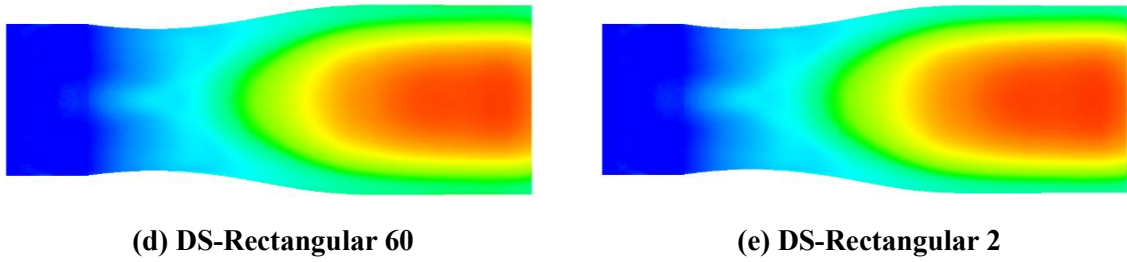


Fig. 9. Wall temperature contours of the DS nozzles.

Figure 10 shows temperature contours on the x -plane of the plume. The plume mixes with the freestream at the nozzle exit, causing a rapid decrease in temperature. The red dotted line represents the gradient dy/dx of the outermost part of the region where the plume temperature was 550 K. The $\tan(dy/dx)$ values for the straight, DS-Elliptic, DS-Rectangular 60, 30, and 2 nozzles were 5.75° , 5.74° , 5.36° , 5.32° , and 5.27° , respectively. Because the mixing of bypass and core flows is higher inside the DS-Elliptic nozzle, the temperature of the plume is reduced more than in the DS-Rectangular nozzle. When the local velocity outside the nozzle exceeds a certain Mach number, a shock wave is formed. The shock wave occurred 1.23 m after the nozzle exit in the straight nozzle. The plume temperature of the double serpentine nozzle decreases faster than that of the straight nozzle. In the double serpentine nozzle, the shock wave formed approximately 0.6 m after the nozzle exit, and the temperature increased by 180 K.

Figure 11 shows the plume temperature and O_2 mole fraction in the x -direction from the nozzle exit center. As the hot spot is created closer to the nozzle exit in the DS nozzles than in the Straight nozzle, the overall temperature of the plume of the DS nozzles is significantly lower. In all Straight, DS-Elliptic, and DS-Rectangular nozzles, the O_2 mole fraction increases rapidly from the point where a hot spot is formed. However, the magnitude of the increase was much larger for DS nozzles, which showed a significantly higher O_2 mole fraction in the entire plume flow field. Although the DS nozzles have higher pressure losses than the Straight nozzle, they mix more efficiently with the free stream outside the nozzle, resulting in a higher O_2 mole fraction, formation of the hot spot closer to the nozzle exit, and decrease in the temperature of the plume.

The effect of the cross-sectional shape on the aerodynamic performance was found negligible. The elliptic cross-sectional shape had little effect on the pressure and negligible impact on the velocity inside the nozzle. The DS-Elliptic and DS-Rectangular nozzles exhibit nearly equivalent impacts on mixing efficiencies and temperature distributions within the plume, indicating minor differences in their performance.

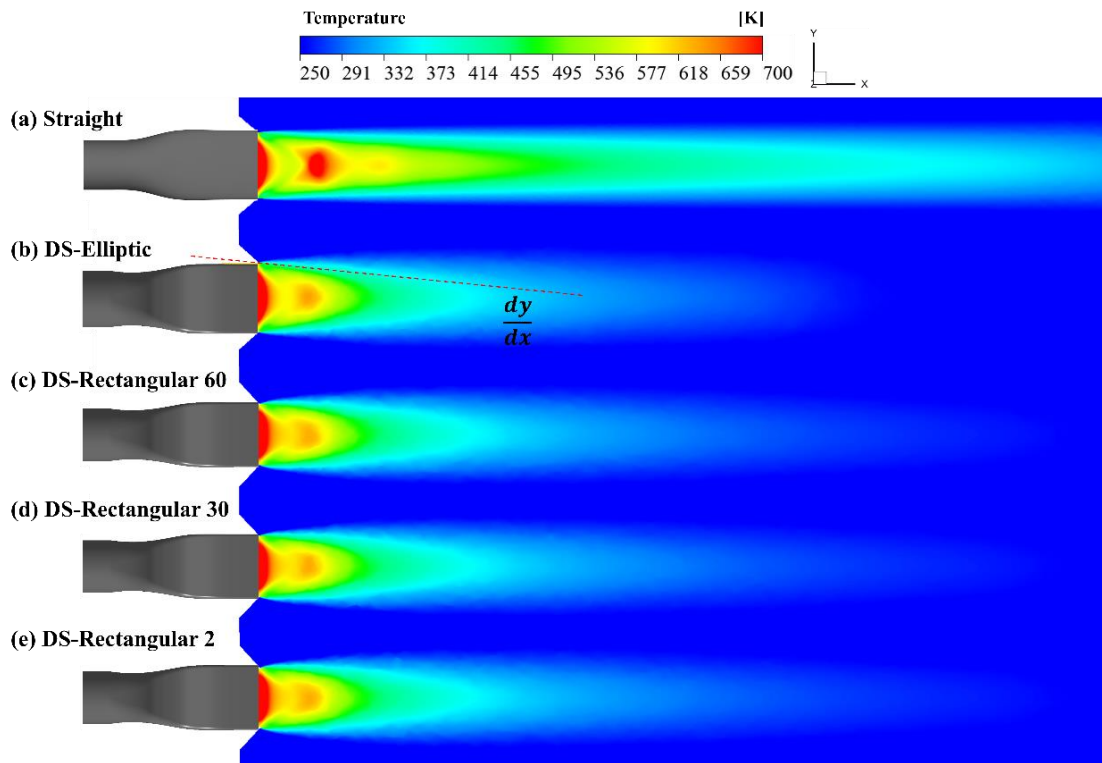


Fig. 10. Temperature contours of the plume.

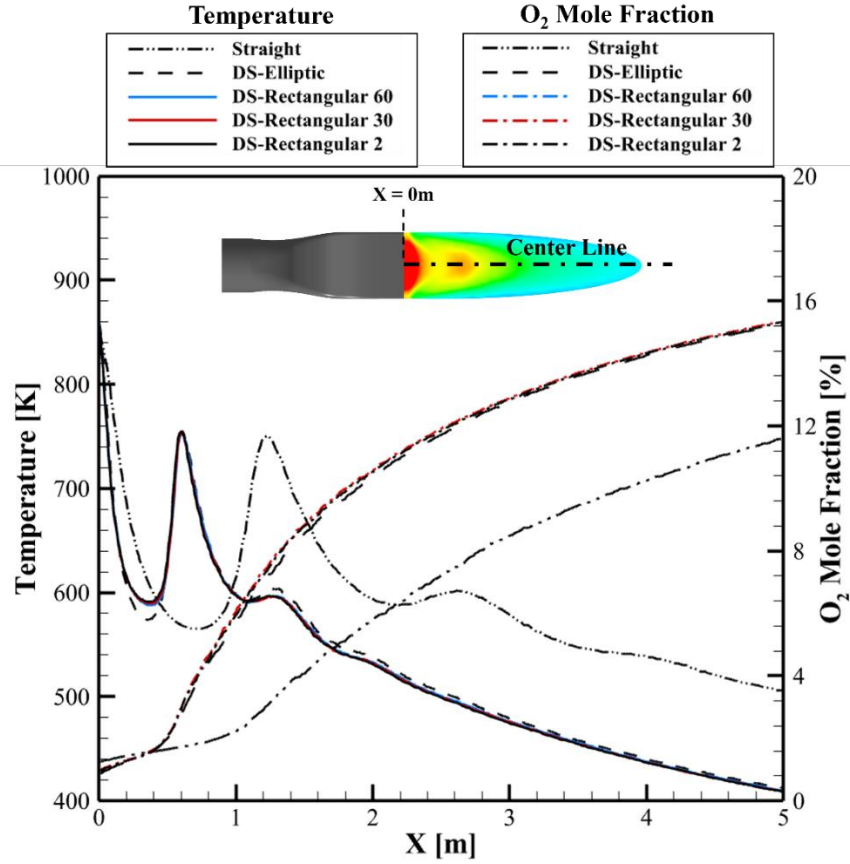


Fig. 11. Temperature and O₂ mole fraction of the plume in the center line.

4. IR signature of the DS nozzles

4.1. Numerical method of computing the IR signature

The radiative heat transfer equation is used to compute the IR signature emitted from the plume. It can be solved based on band models including line-by-line, narrow-band, and wide-band models. The line-by-line model computes the radiative heat transfer equation over the entire wavelength through hundreds of absorption lines in the 25 cm^{-1} wavelength range. Radiant energy can be calculated using a band model that calculates the average radiation properties for the wavelength section. The narrow-band model divides the spectrum, each ranging from 1 to 10 cm^{-1} . The wide-band model divides each band ranging from 100 to $1,000 \text{ cm}^{-1}$. Among the three models, the narrow-band model was adopted in this study because it can calculate IR signatures with relatively high accuracy at a low cost. The narrow-band model is less accurate than the line-by-line model due to approximation errors and spectral overlap but offers greater accuracy compared to the wide-band model.

Absorption and emission radiance, excluding scattering, were computed using a narrow-band model that simulates non-gray gas's transmittance and absorption coefficient. Statistical tables are used for the molecular model and absorption coefficient [38, 39]. Chemical species and temperature of O₂, CO₂, H₂O, and N₂, and thermal flow field are used as input data [40]. Spectral radiance can be calculated for line-of-sight (LOS) between any two points and the 1 to 20 μm wavelength bands using the following equation

$$i'_\lambda(l) = i'_{\lambda,w} e^{-k_\lambda(l)} + \int_0^{k_\lambda(l)} i_{b,\lambda}(l^*) \exp[-(k_\lambda(l) - k_\lambda(l^*))] dk_\lambda(l^*), \quad (4)$$

i'_λ : Spectral radiance,

$i_{b,\lambda}$: Planck blackbody radiance,

$k_\lambda \equiv \int_0^l a_\lambda(l^*) dl^*$: Optical thickness,

a_λ : Spectral absorption coefficient.

In this equation, w , λ , l represent bounding wall condition, wavelength, and characteristic length. Incident-mean absorption coefficient $a_i(l)$ and Planck-mean absorption coefficient $a_p(l)$ are defined as

$$a_i(l) \equiv \int_0^\infty \overline{i_\lambda(l)} a_\lambda(l) d\lambda / i_i(l), \quad (5)$$

$$\text{where, } \overline{i_\lambda(l)} = \frac{1}{4\pi} \int i'_\lambda(l) d\omega$$

$$a_p(l) \equiv \int_0^\infty i_{b,\lambda}(l) a_\lambda(l) d\lambda / i_b(l). \quad (6)$$

Here $i_i(l)$ and $i_b(l)$ appearing in the denominator of each absorption coefficient are incident radiance and blackbody radiance, respectively. ω is the solid angle. Radiative heat transfer is calculated using the data present in the LOS between any two points [41].

4.2. Validation of IR signature prediction code

The present IR signature prediction code was validated based on experimental data of the micro turbojet engine using kerosene as the fuel. The IR signature of the plume was measured at a location one

exit diameter away from the nozzle exit, at an azimuth of 90° . Figure 12 shows the comparison of spectral radiance using circular and serpentine nozzles. Peak signatures are present in $2,000$ to $2,500\text{ cm}^{-1}$ (4 to $5\text{ }\mu\text{m}$) from CO_2 , showing excellent agreement across most spectral regions. In the regions representing the characteristics of H_2O in the plume components, $1,000$ to $2,000\text{ cm}^{-1}$ (5 to $10\text{ }\mu\text{m}$) and 2500 to 4000 cm^{-1} (2.5 to $4\text{ }\mu\text{m}$), the predicted values exhibit somewhat stronger signatures. This discrepancy may be related to the influence of signature absorption in the atmosphere during measurement. In the CFD, the assumption of complete combustion results in higher mole fractions of CO_2 and H_2O compared to the experimental values, leading to a higher IR signature. Additionally, in the experimental environment, the IR signature was absorbed by atmospheric, leading to a higher IR signature in the code compared to the experimental data. In the experiment, a weak signature due to the vibrational mode of CH molecules was detected in the range of $2900\text{--}3000\text{ cm}^{-1}$. However, this mode was not included in the theoretical calculations, so the signature was not present in the simulation results.

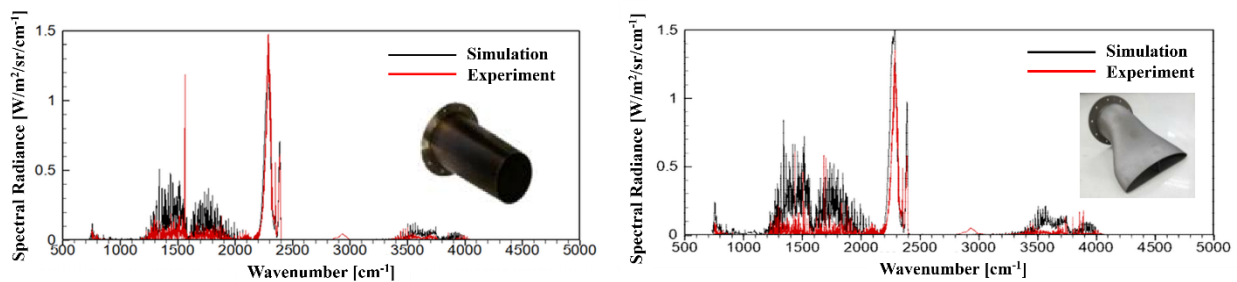


Fig. 12. Comparison of spectral radiance using circular and serpentine nozzles of a micro turbojet engine.

4.3. IR signature of the DS nozzles

The IR signature emitted from the plume was calculated at azimuth and elevation angles (-90° to 90°). Figure 13 shows the spectral radiance for the wavelength band of 1 to $10\text{ }\mu\text{m}$ observed from the rear ($\theta = 0^\circ$) of the nozzle. The maximum spectral radiance occurred at $4.49\text{ }\mu\text{m}$. The spectral radiance of the Straight nozzle was the highest value among all nozzles, at $2103.7\text{ W/m}^2/\mu\text{m/sr}$. The spectral radiance of the DS-Elliptic and DS-Rectangular nozzles was $1,233$ and $1,224\text{ W/m}^2/\mu\text{m/sr}$, respectively. The spectral radiance difference of the DS-Rectangular nozzle due to the change in fillet radius was insignificant. For all nozzles, the highest spectral radiance occurred at $4.49\text{ }\mu\text{m}$, which corresponds to the resonant frequency of CO_2 . The spectral radiance results showed spikes in the 2 to $3\text{ }\mu\text{m}$ and 4 to $5\text{ }\mu\text{m}$ wavelength bands,

which are the resonant frequencies of CO₂ and H₂O [42]. The contribution of the plume is about 10% in the 3 to 5 μm band [43].

Figure 14 shows the IR signature (I/I_{\max}) in azimuth angles. The Straight and DS nozzles exhibited different tendencies at 0 to $\pm 30^\circ$. The IR signature of the DS nozzles was lower than that of the Straight nozzle at the critical azimuth (-30° to 30°). The Straight nozzle showed a maximum IR signature of 77.3% at an azimuth angle of 0° and then it drastically declined until $\pm 30^\circ$. In the DS nozzle, the IR signature increased to $\pm 20^\circ$ and then decreased again. It increased from $\pm 40^\circ$, reached a peak at $\pm 80^\circ$, and then decreased again. The difference in IR signature for the different cross-sectional shapes was within 2% at $\pm 50^\circ$ and reached 9.66% at $\pm 80^\circ$. The DS-Rectangular nozzles have a higher IR signature than the DS-Elliptic nozzle. In the LOS, the DS-Rectangular 2 nozzle has higher temperatures by 5.92 K, 6.367 K, 17.4 K, and 32.03 K at azimuth angles of 0° , 30° , 60° , and 80° , respectively.

Figure 15 shows the IR signature in elevation angle. In the Straight nozzle, the maximum IR signature of 80.73% occurred at $\pm 2^\circ$ and rapidly decreased to 28% around $\pm 15^\circ$. In contrast, in the DS nozzles, the IR signature was found to have high values at 7.5° , 10° , and 12.5° and then decreased sharply to 30% at 15° . This is because, in the DS nozzles, the visible line directly faces the core of the engine at an elevation angle of 7.5° to 12.5° . Additionally, due to the curvature effect of the DS nozzles, it was determined that the elevation angle range with high IR signature was significantly lower than that of the Straight nozzle. An asymmetrical IR signature pattern was also observed in the elevation angle due to the curvature of the DS nozzles, demonstrating the strong influence of their curvature. It can be seen that the curvature effect of the DS nozzles has a significant impact. Table 6 summarizes the angles at which the maximum IR signature (I/I_{\max}) occurs and the values in that direction.

The cross-sectional shape had a limited influence on the maximum IR signature pattern. The cross-sectional shape had little effect on the aerodynamic performance, resulting in slight variations in the IR signature. However, it should be noted that a high shield ratio (≈ 1) may significantly change the aerodynamic performance, potentially resulting in a considerable impact on the IR signature.

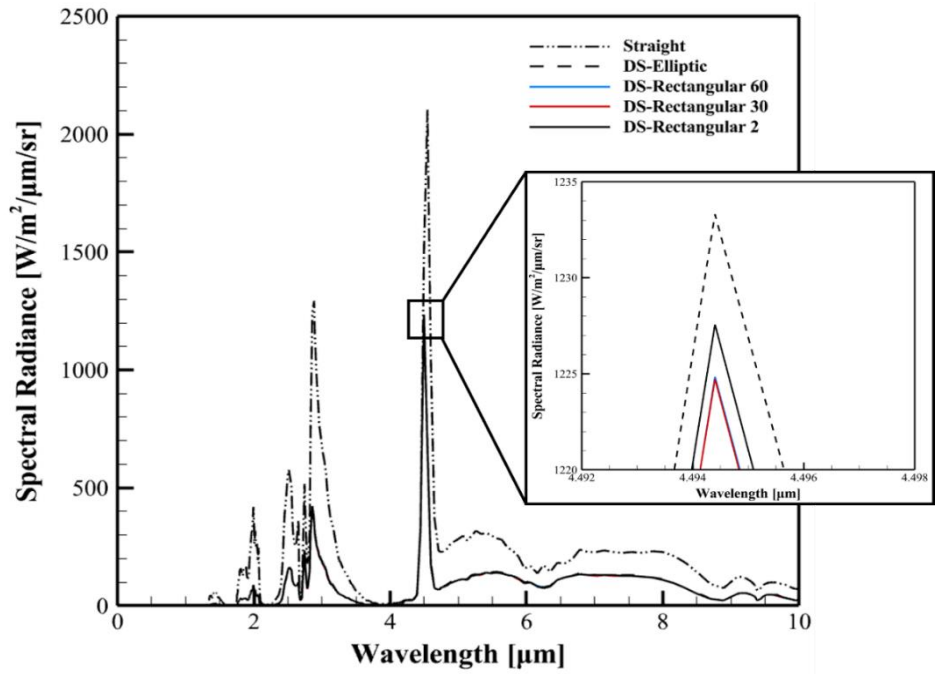


Fig. 13. Spectral radiance by wavelength at 0° for various nozzles.

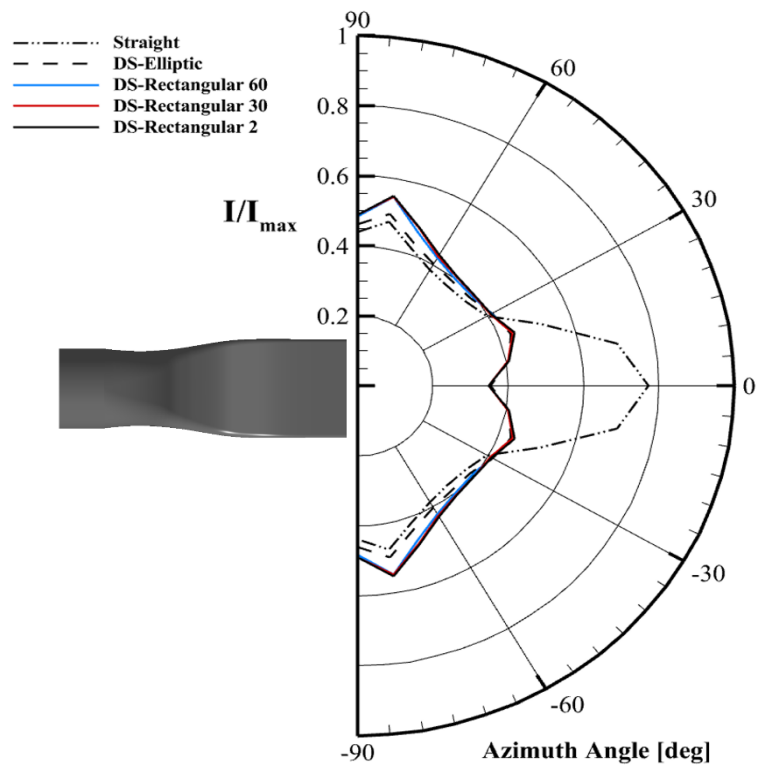


Fig. 14. IR signature in azimuth angle for various nozzles.

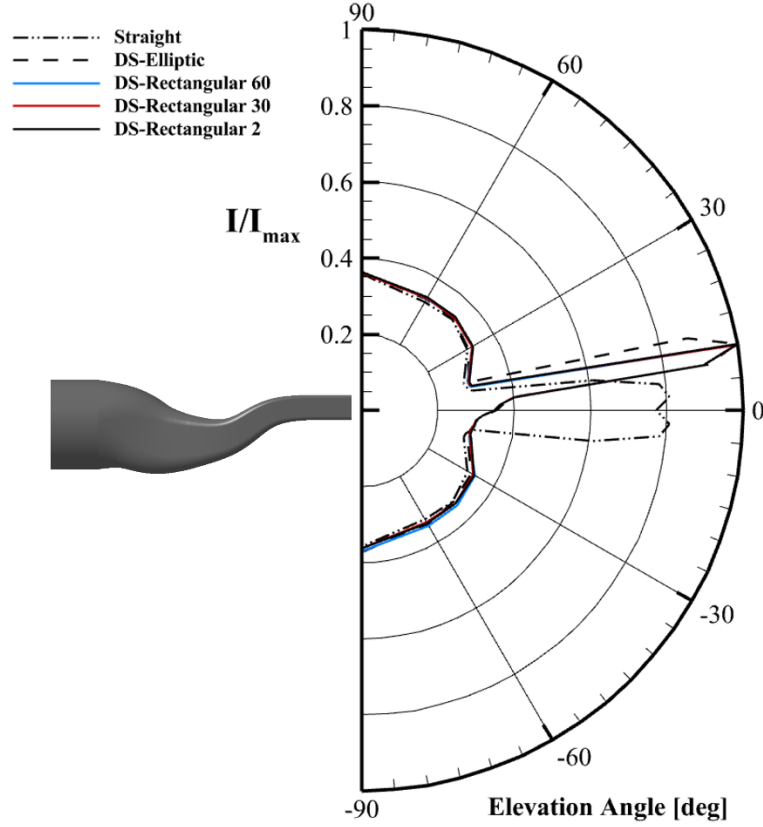


Fig. 15. IR signature in elevation angle for various nozzles.

Table 6 Maximum IR signature in azimuth and elevation angles.

Nozzle	I/I_{\max} (Azimuth Angle)	I/I_{\max} (Elevation Angle)
Straight	0.773 (0°)	0.8073 ($\pm 2.5^\circ$)
DS-Elliptic	0.4978 ($\pm 80^\circ$)	0.9991 (10°)
DS-Rectangular 60	0.5473 ($\pm 80^\circ$)	0.9974 (10°)
DS-Rectangular 30	0.5485 ($\pm 80^\circ$)	0.9976 (10°)
DS-Rectangular 2	0.551 ($\pm 80^\circ$)	1 (10°)

Furthermore, three cases with AR (3, 5, 7) were considered to investigate the effect of aspect ratio on the flow and IR signature of the DS-Elliptic nozzle. Figure 16 shows the pressure recovery and Mach number for the DS-Elliptic nozzles with different AR, while Figs. 17, 18, and Table 7 detail the IR signature. The AR 3 DS-Elliptic nozzle showed a higher overall and maximum IR signature than the AR

5 DS-Elliptic nozzle. The visible line of the AR 3 DS-Elliptic nozzle ranges from 5 to 15°, which is broader than that of the AR 5 DS-Elliptic nozzle. Although the AR 7 DS-Elliptic nozzle showed the highest maximum IR signature at an elevation angle of 10°, it had a lower overall IR signature. However, the AR 7 DS-Elliptic nozzle showed significantly lower pressure recovery than the AR 5 DS-Elliptic nozzle. Thus, the AR showed a clear influence on the IR signature compared to the fillet radius because it causes significant changes in the cross-sectional shape by altering both the minor and major axis radius. The AR 5 DS-Elliptic nozzle showed a balanced performance in terms of both flow and IR signature.

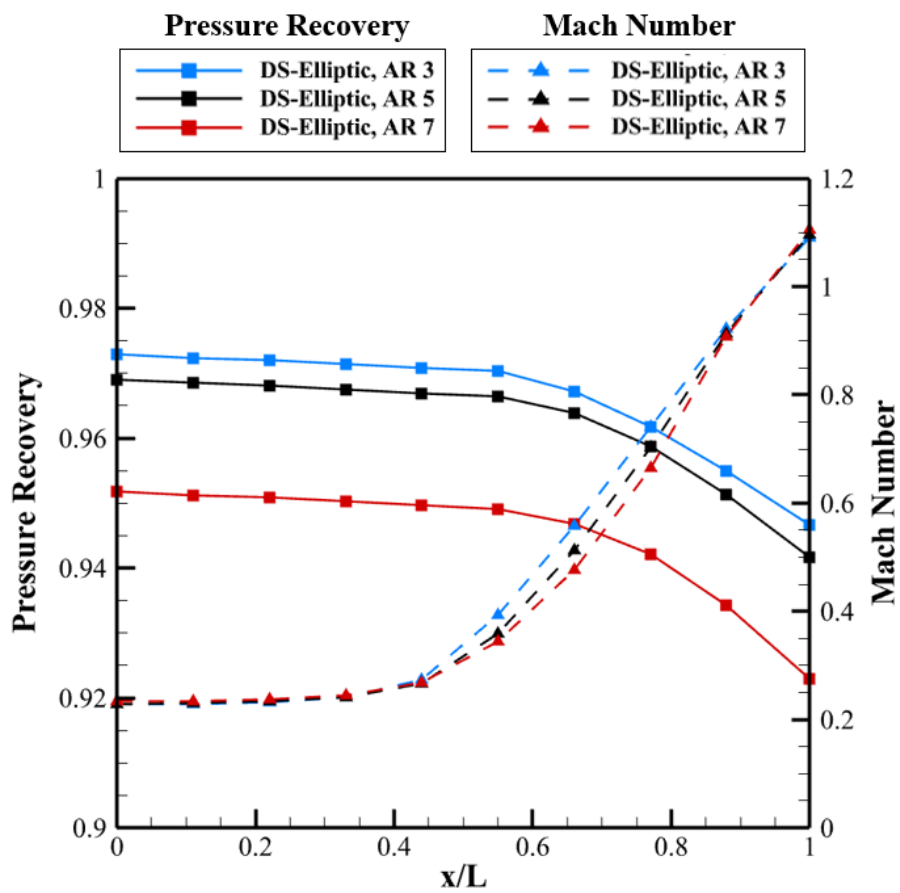


Fig. 16. Pressure recovery and Mach number distribution at the nozzles with AR.

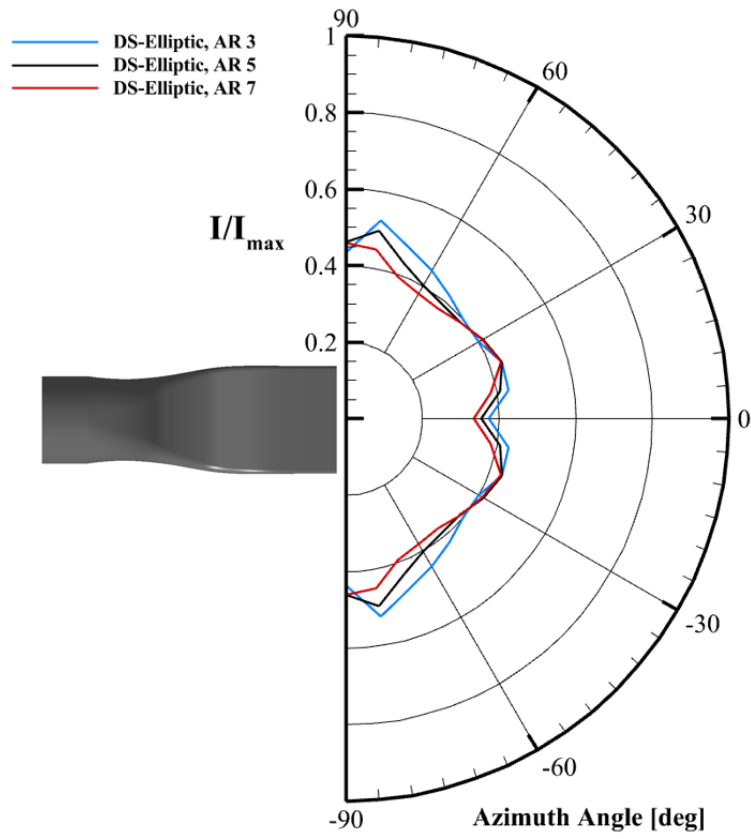


Fig. 17. IR signature in azimuth angle for DS-Elliptic nozzles with AR.

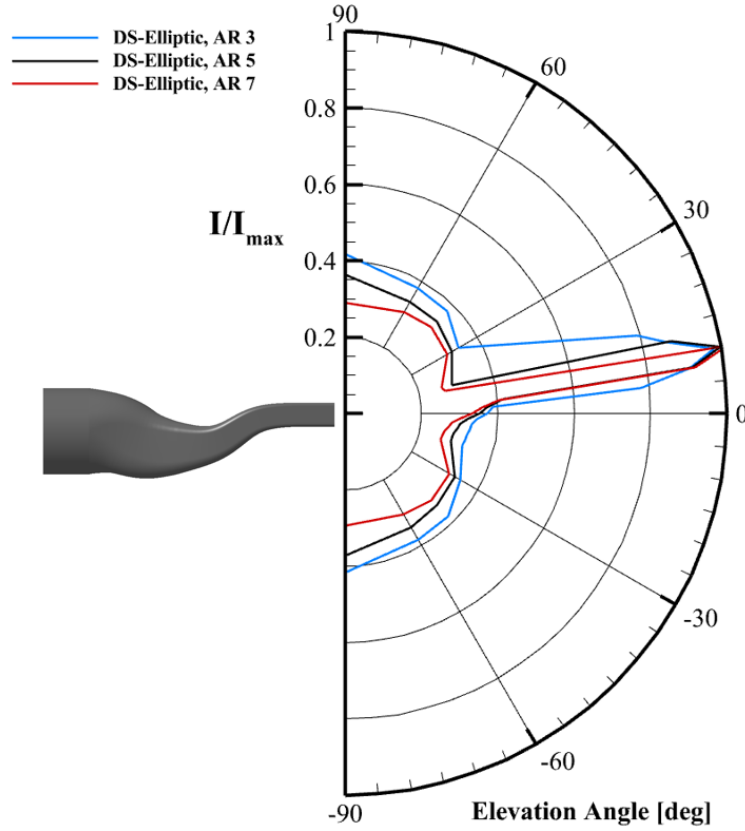


Fig. 18. IR signature in elevation angle for DS-Elliptic nozzles with AR.

Table 7 Maximum IR signature of the DS-Elliptic nozzles with AR.

Nozzle	I/I _{max} (Azimuth Angle)	I/I _{max} (Elevation Angle)
DS-Elliptic, AR 3	0.5259 (± 80°)	0.9825 (10°)
DS-Elliptic, AR 5	0.4978 (± 80°)	0.9991 (10°)
DS-Elliptic, AR 7	0.4901 (± 80°)	1.015 (10°)

5. RCS of the DS nozzles

5.1. Numerical methods of calculating RCS based on full Maxwell equations

To calculate the RCS of the DS nozzles, the present study employed a computational solver based on the following full Maxwell's equations:

$$\int_{\partial\Sigma} \mathbf{E} \cdot d\mathbf{l} = -\frac{d}{dt} \iint_{\partial\Omega} \mathbf{B} \cdot d\mathbf{S}, \quad (7)$$

$$\int_{\partial\Sigma} \mathbf{H} \cdot d\mathbf{l} = \frac{d}{dt} \iint_{\partial\Omega} \mathbf{D} \cdot d\mathbf{S} + \iint_{\partial\Omega} \mathbf{J} \cdot d\mathbf{S}, \quad (8)$$

$$\iint_{\partial\Omega} \mathbf{D} \cdot d\mathbf{S} = \iiint_{\Omega} \rho dV, \quad (9)$$

$$\iint_{\partial\Omega} \mathbf{B} \cdot d\mathbf{S} = 0, \quad (10)$$

$$\iint_{\partial\Omega} \mathbf{J} \cdot d\mathbf{S} = -\frac{d}{dt} \iiint_{\Omega} \rho dV. \quad (11)$$

These equations represent the integral form of Maxwell's equations. All integrals on the left-hand side of the five equations are closed line or surface or volume integrals. \mathbf{E} , \mathbf{D} , \mathbf{H} , \mathbf{B} , and \mathbf{J} represent the electric field intensity, the electric flux density, the magnetic field intensity, the magnetic flux density, and the total electric current density, respectively. ρ is total electric charge density. Σ and Ω represent two-dimensional surfaces and three-dimensional volumes.

The method of moments (MoM), also known as the moment method, is a powerful numerical technique for solving the electromagnetic scattering problem [44]. It is a full-wave solver that has the

advantage of accurately calculating electromagnetic wave scattering characteristics such as scattering at the edge, diffraction, and creeping waves. The basic principle of the moment method is to convert an integral form of the full Maxwell's equation, through numerical approximations, into a matrix equation that can be solved numerically.

However, since this fully populated system matrix is computationally very time-consuming, so-called fast solvers are further needed to solve large-scale electromagnetic wave problems, especially the scattering problem [42]. Among various fast solvers, the multilevel fast multipole method (MLFMM) stands out for its high efficiency. The fast multipole method (FMM) was originally proposed to evaluate particle interactions and solve static integral equations rapidly. Based on the fact that calculating a matrix-vector product in the moment method is equivalent to calculating the mutual interaction between a set of current elements, the basic idea of FMM is to first divide the current elements into groups based on their physical location in space and introduce a hub, which is a collection of the current elements that are close to each other. Once the elements are connected within the same group to a single hub and the hubs are connected, the number of computations can be greatly reduced. Efficiency can be further increased by establishing another layer of hubs, leading to a multilevel fast method.

In the present study, FEKO's MoM-MLFMM module was used to calculate the RCS of the double serpentine nozzle, especially multiple reflections inside the nozzle. FEKO is a general-purpose 3D electromagnetic (EM) simulator developed by Altair Engineering [45].

5.2. Validation of the RCS numerical method

To validate the RCS numerical method (MoM-MLFMM), we first considered NASA's almond shape with a length of 0.252m [46]. Mono-static RCS was calculated for azimuth angles 0° to 180° . The frequency was set to 9.92 GHz with vertical transmit-vertical receive (VV) and horizontal transmit-horizontal receive (HH) polarization [47]. Figure 19 shows the RCS results for the almond shape. The computational results show excellent agreement with the experimental data.

We then considered a cylinder shape with an open-ended cavity structure that was identical in terms of topology to the aircraft nozzle geometry [48]. The diameter (D) and length (L) of the cylinder are four times ($D = L = 4\lambda$). The frequency was set to 10GHz; equivalently, the wavelength, $\lambda \approx 3$ cm. Figure 20

shows the electromagnetic wave scattering characteristics of the open-ended cavity structure in the case of mono-static radar. The results confirmed that both VV and HH-polarization results were in close agreement with the modal reference solutions.

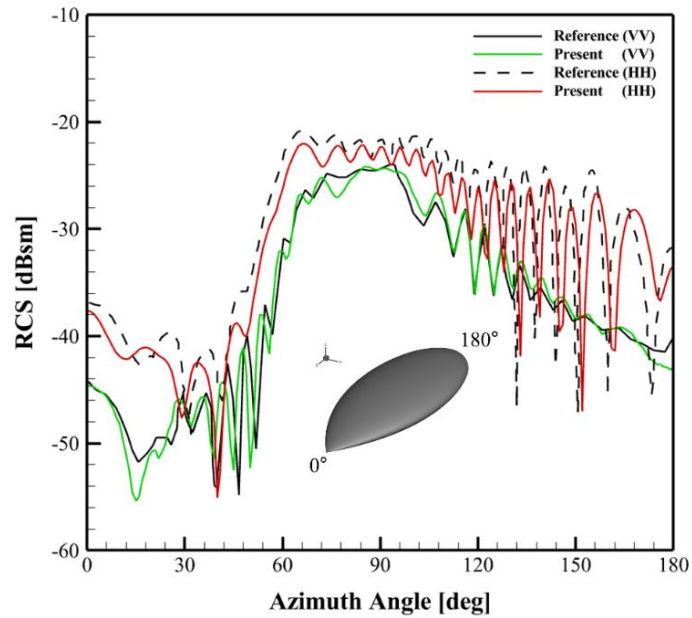


Fig. 19. RCS validation of NASA almond.

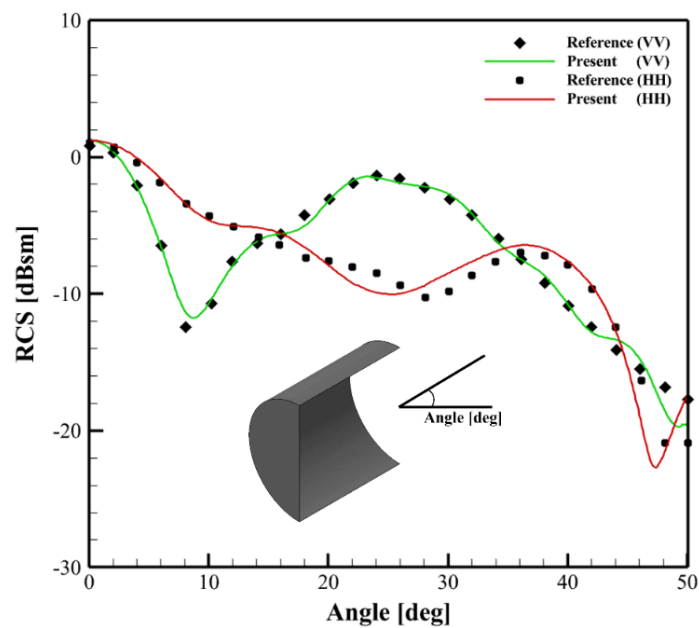


Fig. 20. RCS validation of open-ended cavity.

5.3 Conditions for RCS calculation

We assume the cruise condition at an altitude of 12 km. The radar distance, which radiates radio waves with a frequency of 10 GHz, was chosen to be at least 150 km to determine the detection angle. Azimuth angles of -45° to 45° and elevation angles of -5° to 5° with an interval of 1° were considered. Other detailed information is summarized in Table 8.

The MLFMM computational solver was used to compute the RCS inside the DS nozzles. The average length of the surface grid of the nozzle was chosen to be $1/16$ of the wavelength. Since the nozzle is mounted internally on the aircraft, there is no need to calculate RCS for the external surface of the nozzle. A computational zone that completely absorbs electromagnetic waves was imposed on the external surface of the nozzle. To prevent reflections from the surface, the zone was simulated by setting its surface with an impedance similar to air and a high electromagnetic loss tangent value. To check the effectiveness of such a radar absorbing zone, it was applied to a plate ($150\text{mm} \times 150\text{mm} \times 10\text{mm}$) with a value of 20.5dBsm in the case of a perfect electrical conductor (PEC), and it was found that it had a very low value of -25.2 dBsm. In contrast, a PEC condition is imposed on the inner surface of the nozzle.

Table 8. Conditions for RCS calculation

Radar Systems Parameter	Conditions
Radar Type	Mono-static Radar
Frequency	10 GHz
Azimuth Angle	-45° to 45°
Elevation Angle	-5° to 5°
Interval	1°
Polarization	VV, HH

5.4 Current distribution on the inner surface of the DS nozzles

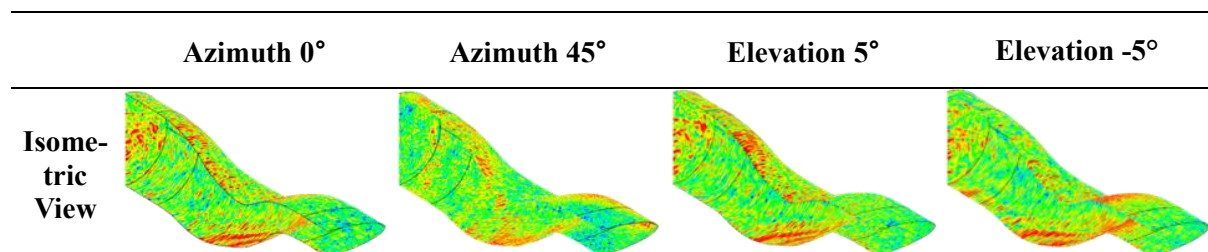
Surface currents are electric currents induced on the nozzle surface by electromagnetic waves. It can be used to analyze the positions of incident and reflected electromagnetic waves within the nozzle.

Figure 21 shows the current distribution on the inner surface of the DS-Elliptic nozzle for VV-polarization, azimuth angles 0° , 45° , and elevation angles $\pm 5^\circ$. The figure shows the half-shaped cut in the ZX plane of the nozzle and isometric, front, behind, top, and bottom views. The inner surface current is a value of -60 to -40 to highlight the surface of the nozzle where the current is concentrated.

At 0° , the highest inner surface current appears on the upper surface because the electromagnetic wave first encounters the upper surface of the nozzle in center curve 2, as indicated in Fig. 2. The reflected electromagnetic wave then hits the lower surface, resulting in a high inner surface current on the lower surface of center curve 2. From there, the electromagnetic waves experience multiple bounces inside the nozzle, generating a uniform current, and are encountered in the center of the inlet of the nozzle.

At an azimuth angle of 45° , the highest inner surface current appears at the corner of the major axis of the nozzle exit and develops asymmetrically to the left and right. The inner surface current inside the nozzle is higher than at other angles. At elevation angle -5° , the inner surface current is more concentrated on the upper and lower surface of center curve 2 than 0° . This is because the angle at which the electromagnetic waves hit the upper surface significantly influences its intensity. As a result, there is an increase in electromagnetic waves that are refracted and reflected towards the lower surface. In contrast, at elevation 5° , there is a relatively weak inner surface current because the intensity of the electromagnetic wave hitting the wall is not strong. The inner surface current distributed at the nozzle inlet is the lowest, which can reduce multiple bounces in the engine.

Figure 22 shows the inner surface current for different cross-sectional shapes of a DS nozzle at 0° (VV-polarization). The DS-Rectangular nozzles have a wider distribution of high-intensity currents compared to the DS-Elliptic nozzle, resulting in overall higher inner surface currents. Furthermore, the DS-Rectangular nozzles generate high currents at the edges. These differences in distribution are due to the flat surfaces and distinct rectangular edges, which increase reflection and scattering. Additionally, the DS-Rectangular nozzle's high-intensity currents are concentrated more at the center of the nozzle inlet than those of the DS-Elliptic nozzle. Thus, the reflection characteristics of electromagnetic waves are significantly influenced by the cross-sectional shape of the nozzle.



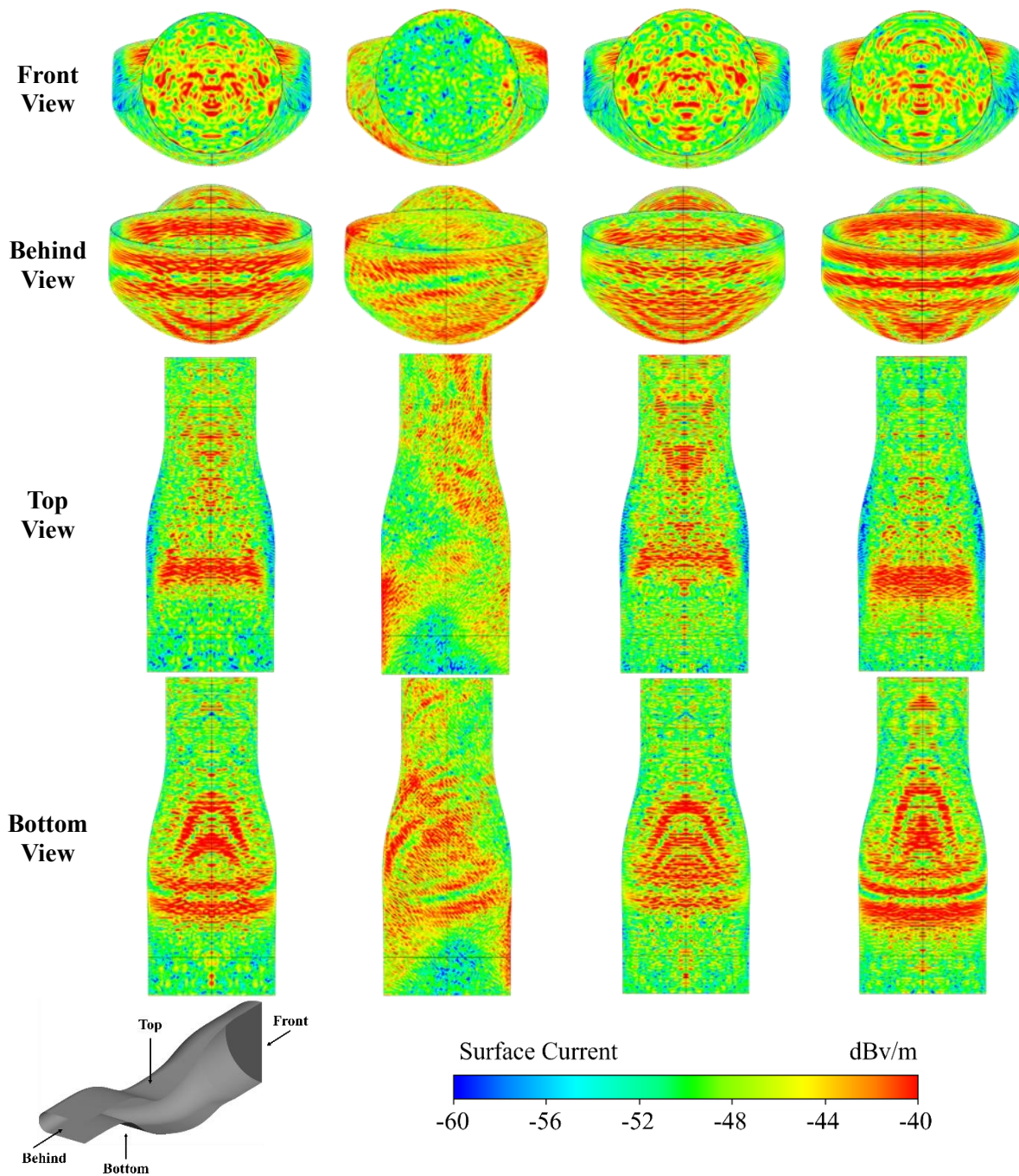
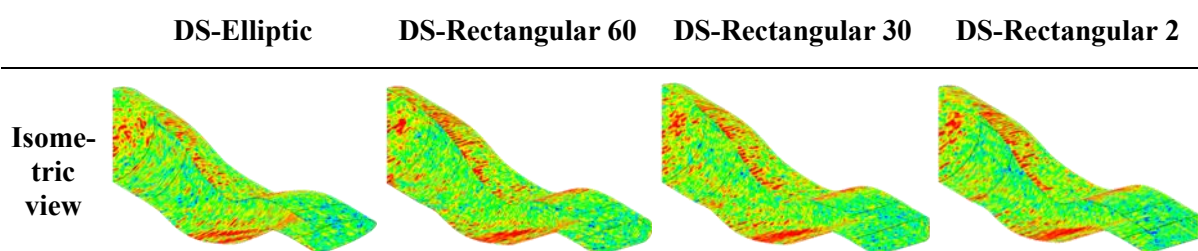


Fig. 21. Current distribution on the inner surface of the DS-Elliptic nozzle.



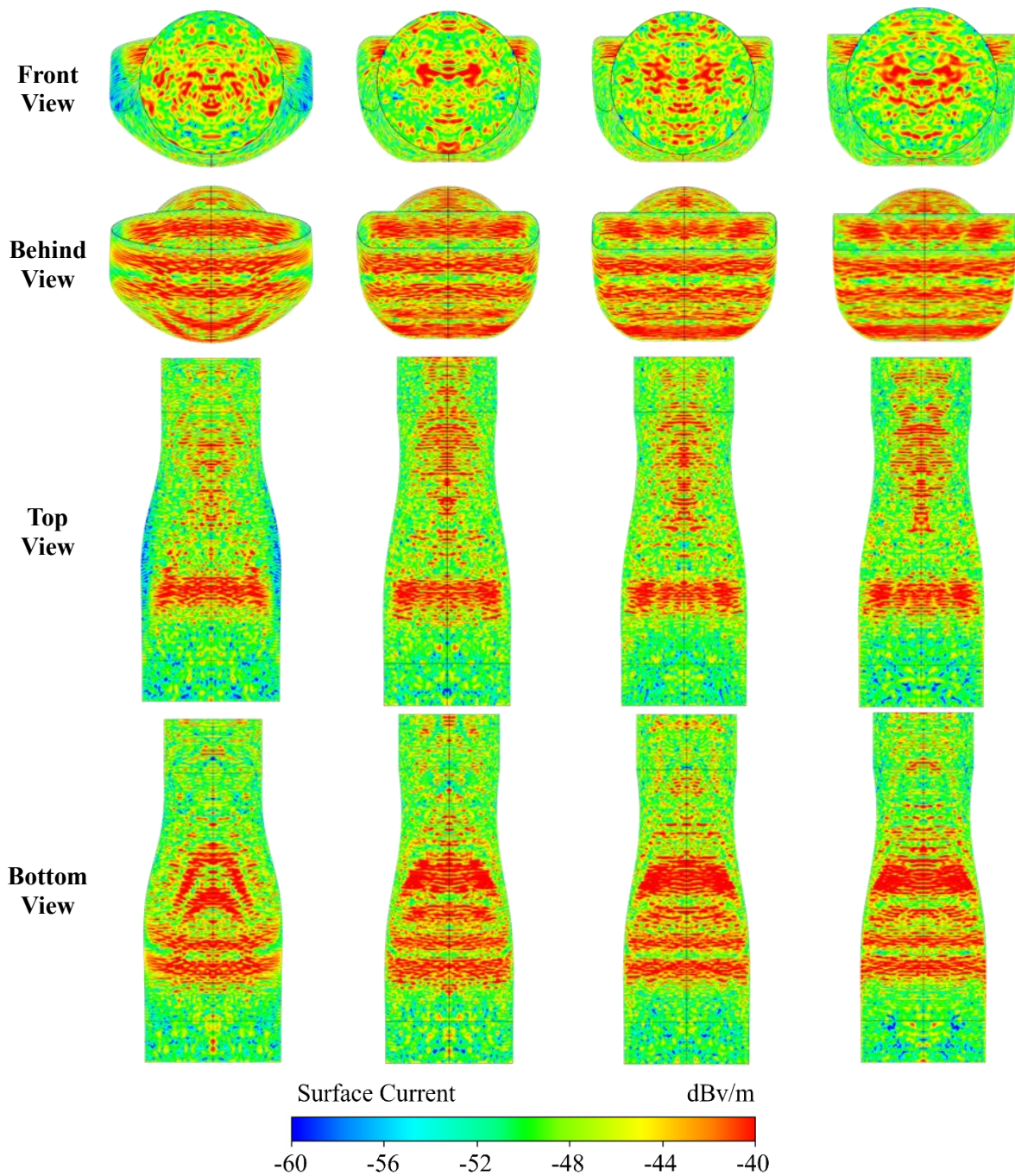


Fig. 22. Current distribution on the inner surface of various nozzles.

5.5 RCS of the DS nozzles

Figure 23 and Table 9 show the RCS in the azimuth angle (VV-polarization). Maximum RCS, arithmetic mean RCS, and geometric mean RCS were compared and analyzed. RCS can be expressed in $[m^2]$ or $[dBsm]$. The arithmetic mean RCS is calculated by averaging the RCS values in $[m^2]$ and then

converting them to [dBsm]. In contrast, the geometric mean RCS is calculated by converting the RCS values to [dBsm] first and then averaging them [49]. Large RCS values significantly affect the arithmetic mean RCS values, whereas small RCS values significantly affect the geometric mean RCS. To reduce the radar detection range, the difference between the two average RCSs must be reduced.

The maximum RCS of the straight nozzle was 10.31 dBsm at 0° . The arithmetic and geometric mean RCS were 1.693 and -1.988 dBsm, respectively. In the double serpentine nozzles, RCS was significantly reduced due to multiple reflections inside the nozzle. The maximum RCS of the DS-Elliptic and DS-Rectangular 60, 30 nozzles were 0.8103, 8,096, and 1.855 dBsm, respectively, at 0° . The DS-Elliptic nozzle has an evenly curved surface that scatters electromagnetic waves, resulting in a low RCS. In contrast, the DS-Rectangular 60 nozzle has flat and wide surfaces that create a larger area for reflection. Additionally, the large fillet radius complicates internal reflection paths, significantly increasing the RCS at 0° .

The RCS of the DS-Elliptic and DS-Rectangular 60 nozzles tended to decrease as the azimuth angle increased after the maximum RCS occurred at 0° . However, the RCS of the DS-Rectangular 30 nozzle increased after $\pm 10^\circ$ and decreased after a large RCS at $\pm 30^\circ$. The DS-Rectangular 2 nozzle also had a large RCS at 0° , but the maximum RCS was 4.227 dBsm at $\pm 30^\circ$.

Among the double serpentine nozzles, the DS-Elliptic nozzle had the lowest geometric mean RCS (-10.37dBsm), while the DS-Rectangular 2 nozzle had the highest RCS (-6.109dBsm), a difference of 4.260 dBsm. In addition, in the arithmetic mean RCS, the DS-Elliptic nozzle exhibited a value of 5.175dBsm lower than the DS-Rectangular 2 nozzle, which is a significant difference. The largest difference between the two mean RCS was for the DS-Rectangular 2 nozzle, with a difference of 2.472 dBsm.

Figure 24 and Table 10 show the results of HH-polarization, which were similar to that of VV-polarization. The maximum RCS of the straight nozzle was 10.01 dBsm at 0° . The arithmetic and geometric mean RCS were -0.9278 and 2.444 dBsm, respectively. The double serpentine nozzles had a lower RCS than the straight nozzle. The maximum RCS were 0.8103, 2.630, and 5.804 dBsm at 0° for the DS-Elliptic and the DS-Rectangular 60, 30 nozzles, respectively, while it was 2.756 dBsm at $\pm 30^\circ$ for the DS-Rectangular 2 nozzle. The geometric and arithmetic mean RCS (-6.331 and -4.446 dBsm, respectively)

were the highest in the DS-Rectangular 2 nozzle. The largest difference between the two mean RCS was observed for the DS-Rectangular 2 nozzle, at 1.885 dBsm.

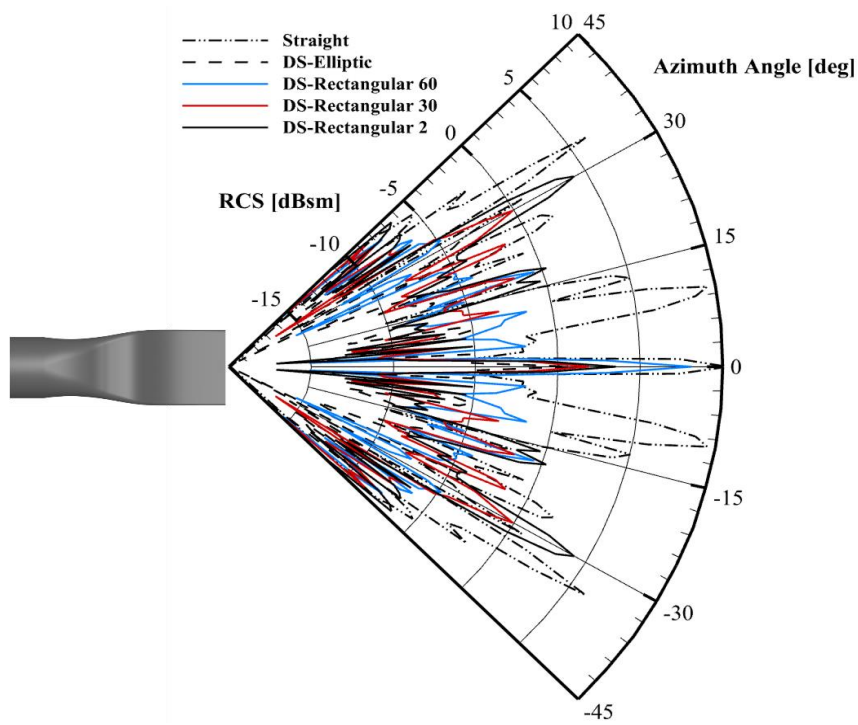


Fig. 23. RCS of DS nozzles in azimuth angle (VV-polarization).

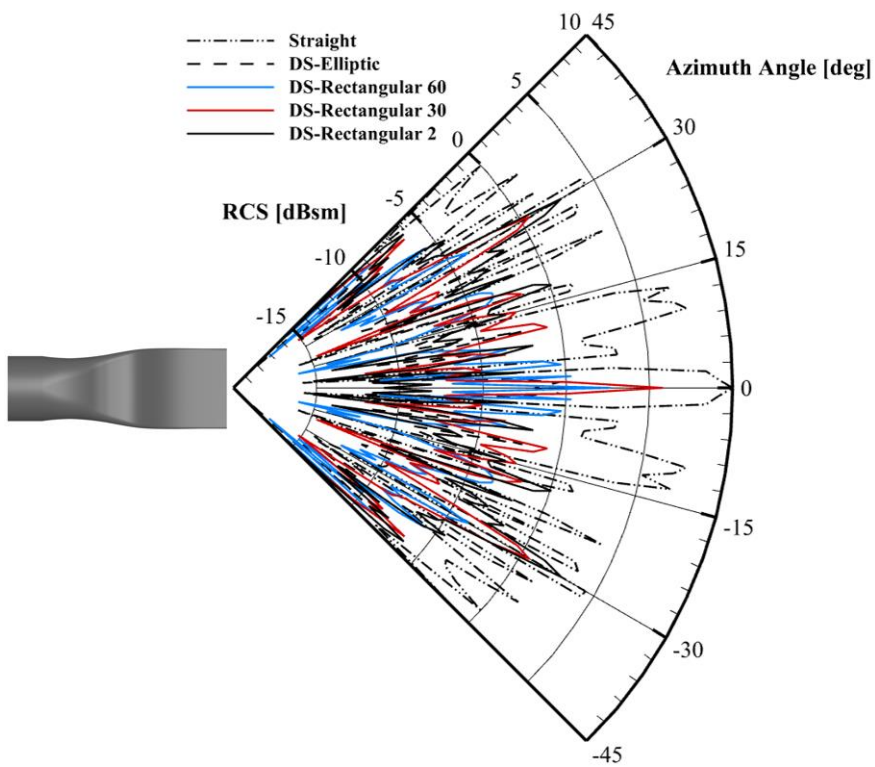


Fig. 24. RCS of DS nozzles in azimuth angle (HH-polarization).

Table 9 RCS of DS nozzles in azimuth angle (VV-polarization).

Nozzle	Maximum RCS [dBsm]	Arithmetic Mean RCS [dBsm]	Geometric Mean RCS [dBsm]
Straight	10.31 (0°)	1.693	-1.988
DS-Elliptic	0.8103 (0°)	-8.815	-10.37
DS-Rectangular 60	8.096 (0°)	-4.406	-6.711
DS-Rectangular 30	1.855 (0°)	-5.524	-7.018
DS-Rectangular 2	4.227 (30°)	-3.637	-6.109

Table 10 RCS of DS nozzles in azimuth angle (HH-polarization).

Nozzle	Maximum RCS [dBsm]	Arithmetic Mean RCS [dBsm]	Geometric Mean RCS [dBsm]
Straight	10.01	-0.9278	2.444
DS-Elliptic	0.8103 (0°)	-21.49	-10.37
DS-Rectangular 60	2.630 (0°)	-6.066	-7.906
DS-Rectangular 30	5.804 (0°)	-4.598	-6.435
DS-Rectangular 2	2.756 (30°)	-4.446	-6.331

Figure 25 and Table 11 show the RCS in the elevation angle (VV-polarization). The maximum RCS of the straight nozzle was 10.31 dBsm at 0°. The arithmetic and geometric mean RCS were 9.582 and 9.612 dBsm, respectively. The symmetrical straight nozzle generated a higher RCS than the double serpentine nozzles at 0°. The maximum RCS of the DS-Elliptic and DS-Rectangular 60, 30, and 2 nozzles were 0.3848, 8.096, 5.365, and 3.376 dBsm, respectively, but occurred at different elevation angles. It occurred near 0° for the DS-Elliptic and DS-Rectangular 60 nozzles, while it occurred at ± 5° for the DS-Rectangular 30 and 2 nozzles. The arithmetic and geometric RCS (2.689 and 4.588 dBsm, respectively) were the largest in the DS-Rectangular 60 nozzle. The difference between the two mean RCS was largest for the DS-Rectangular 30 nozzle, at 2.862 dBsm. The lowest maximum mean RCS was for the DS-Elliptic nozzle.

Figure 26 and Table 12 show the RCS in the elevation angle (HH-polarization). The maximum RCS of the straight nozzle was 10.01 dBsm at 0°. The maximum RCS of the DS-Elliptic and DS-Rectangular 60, 30, and 2 nozzles were 7.756, 5.916, 6.389, and 1.221 dBsm, respectively. The maximum RCS of the double serpentine nozzles occurred at 5° except for the DS-Rectangular 30 nozzle (1°). The largest arithmetic and geometric RCS (3.624 and 2.711 dBsm, respectively) were observed in the DS-Rectangular 30 nozzle. The largest difference between the two mean RCS was for the DS-Rectangular 2 nozzle with a difference of 3.161 dBsm.

The cross-sectional shape of DS nozzles has a significant impact on the RCS. First, the DS-Rectangular nozzles have a large and flat surface area that significantly reflects electromagnetic waves, resulting in a high RCS. Second, the distinct rectangular edges increase reflection and scattering, causing strong backscatter when electromagnetic waves hit perpendicularly. Additionally, the DS-Rectangular nozzle's surface currents are more concentrated near the edges, leading to stronger reflections and further increasing the overall RCS. To reduce RCS, it is essential to analyze not only the RCS values but also the surface current, aiding in the nozzle design to enhance low-observable characteristics by minimizing RCS.

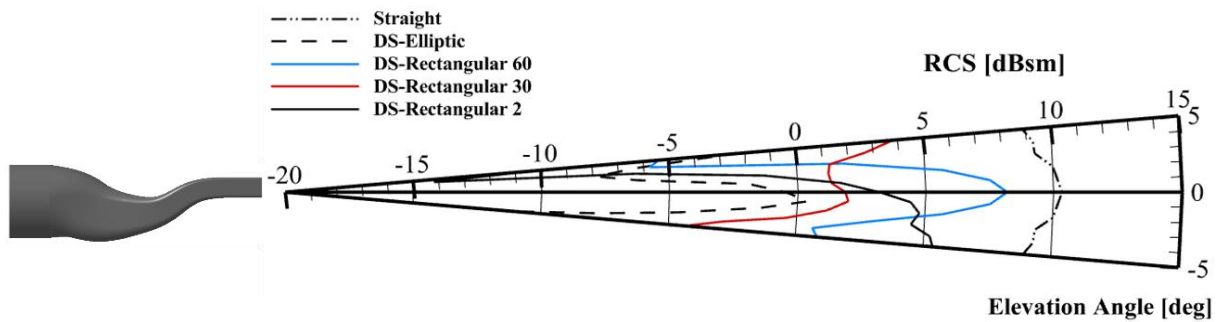


Fig. 25. RCS of DS nozzles in elevation angle (VV-polarization).

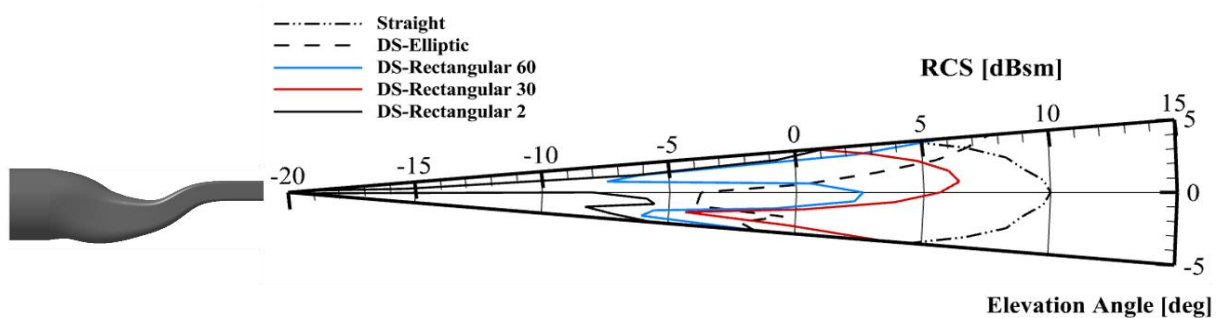


Fig. 26. RCS of DS nozzles in elevation angle (HH-polarization).

Table 11 RCS of DS nozzles in elevation angle (VV-polarization).

Nozzle	Maximum RCS [dBsm]	Arithmetic Mean RCS [dBsm]	Geometric Mean RCS [dBsm]
Straight	10.31 (0°)	9.582	9.612
DS-Elliptic	0.3848 (-1°)	-3.312	-4.519
DS-Rectangular 60	8.096 (0°)	4.588	2.689
DS-Rectangular 30	5.365 (-5°)	2.593	-0.2691
DS-Rectangular 2	3.376 (5°)	1.180	0.6777

Table 12 RCS of DS nozzles in elevation angle (HH-polarization).

Nozzle	Maximum RCS [dBsm]	Arithmetic Mean RCS [dBsm]	Geometric Mean RCS [dBsm]
Straight	10.01 (0°)	7.820	8.197
DS-Elliptic	7.756 (5°)	2.781	0.7096
DS-Rectangular 60	5.916 (5°)	0.6782	-1.207
DS-Rectangular 30	6.389 (1°)	3.624	2.711
DS-Rectangular 2	1.221 (5°)	-4.680	-7.841

6. Conclusions

In this study, we investigated how the cross-sectional shape affected all three characteristics of thrust and pressure recovery, IR signature, and radar cross section (RCS) with surface current, which are associated with the propulsive performance and low observability of DS nozzles.

Firstly, the 3D compressible Reynolds-averaged Navier-Stokes equations were used to compute the thermal flow field of the plume in the DS nozzles. The DS-Elliptic nozzle had better performance in

pressure recovery for all except the Straight nozzle. The thrusts of the different cross-sectional shapes only varied within 0.67%, and consequently, the shape had little effect on thrust performance.

Secondly, the IR signature was analyzed using the radiative heat transfer equation with a narrow band model. The wall temperature of the DS-Elliptic nozzles turned out to be lower, effectively reducing the plume temperature. The maximum IR signature for all DS nozzles occurred at an elevation angle of 10° , due to the curvature. In addition, the range of critical elevation angles with high IR signatures was smaller compared to the Straight nozzle. The IR signature of the DS-Elliptic nozzle was lower than that of the DS-Rectangular nozzle at the critical azimuth (-30° to 30°), demonstrating the superior performance of the DS-Elliptic nozzle in reducing the IR signature of the plume (reducing the maximum IR by up to 9.66%).

Lastly, the RCS was calculated using a multi-level fast multipole method of full Maxwell's equations that can calculate multiple bounces inside the DS nozzles for entire angles, instead of the approximate methods often employed. As expected, the Straight nozzle produced the largest RCS in all aspects (maximum, arithmetic, and geometric mean). Among the DS nozzles, the mean RCS was largest in azimuth angle for DS-Rectangular 2, while the mean RCS was largest in elevation angle for the DS-Rectangular 60 nozzle (VV-polarization) and the DS-Rectangular 30 nozzle (HH-polarization). The flat surface of the DS-Rectangular nozzles tends to increase RCS, so the DS-Elliptic nozzle performed best in reducing RCS in almost all cases (reducing the maximum RCS by up to 90% and the mean RCS by up to 383%).

Overall, the present study shows that cross-sectional shape has different levels of impact on thrust and pressure recovery (negligible), IR signature (limited), and RCS (significant). In the next study, we will explore in depth the effects of the nozzle cross-sectional and exit shape on aerodynamic and propulsive performance and low observability, including the effects of solid IR, for a full UCAV with the afterdeck and DS nozzles internally mounted. Such a study can offer insights into the design of low-observable UCAVs while minimizing associated penalties and considering constraints like manufacturability.

Acknowledgment

This work was supported by a research contract (UD2100251D) and the Aerospace Low Observable Technology Laboratory Program (UD20003JD) of the Agency for Defense Development of the Republic of Korea. The authors would like to thank Yu-Ryeol Lee of Korea Aerospace Industries, Ltd. for his help with electromagnetic field calculations.

Reference

- [1] R. Austin, *Unmanned Aircraft Systems: UAVS Design, Development and Deployment*, A John Wiley and Sons, Wiltshire. (2010) 71.
- [2] G. Wang, L. Guo, H. Duan, L. Liu, H. Wang, A modified firefly algorithm for UCAV path planning, *International Journal of Hybrid Information Technology*. 5 (3) (2012) 123-144. <https://doi.org/10.21236/ada566304>.
- [3] A. Papageorgiou, M. Tarkian, K. Amadori, J. Ölvander, Multidisciplinary optimization of unmanned aircraft considering radar signature, sensors, and trajectory constraints, *Journal of Aircraft*. 55 (4) (2018) 1629-1640. <https://doi.org/10.2514/1.C034314>.
- [4] R.E. Ball, *The Fundamentals of Aircraft Combat Survivability Analysis and Design*, 2nd ed., AIAA, Virginia, 2003. <https://doi.org/10.2514/4.862519>.
- [5] J.R. Teague, D. Schmieder, *The History of Forward-Looking Infrared (FLIR)*, Defense Systems Information Analysis Center (DSIAC), Belcamp, 2021.
- [6] H.R. Sonawane, S.P. Mahulikar, Effect of missile turn rate on aircraft susceptibility to infrared-guided missile, *Journal of Aircraft*. 50 (2) (2013) 663-667. <https://doi.org/10.2514/1.C031902>.
- [7] A. Antonakis, T. Nikolaidis, P. Pilidis, Effects of propulsion system operation on military aircraft survivability, *Journal of Aircraft*. 56 (6) (2019) 2131-2143. <https://doi.org/10.2514/1.C035508>.
- [8] J.R. White, *Aircraft Infrared Principles, Signatures, Threats, and Countermeasures*, Naval Air Warfare Center Weapons DIV, China Lake, CA, 2012, pp.33-61.
- [9] G.A. Rao, S.P. Mahulikar, Effect of atmospheric transmission and radiance on aircraft infrared signatures, *Journal of Aircraft*. 42 (4) (2005) 1046-1054. <https://doi.org/10.2514/1.7515>.
- [10] S.P. Mahulikar, R.S. Hemant, R. Arvind, Infrared signature studies of aerospace vehicles, *Progress in Aerospace Science*. 43 (2007) 218-245. <https://doi.org/10.1016/j.paerosci.2007.06.002>.
- [11] H.T. Anastassiou, A review of electromagnetic scattering analysis for inlets, cavities, and open ducts, *IEEE Antennas and Propagation Magazine*. 45 (6) (2003) 27-40. <https://doi.org/10.1109/MAP.2003.1282177>.
- [12] Y. He, Q. Yang, X. Gao, Comprehensive optimization design of aerodynamic and electromagnetic

- scattering characteristics of serpentine nozzle, *Chinese Journal of Aeronautics*. 34 (3) (2021) 118-128. <https://doi.org/10.1016/j.cja.2020.10.010>.
- [13] W. Cheng, Z. Wang, L. Zhou, X. Sun, J. Shi, Influences of shield ratio on the infrared signature of serpentine nozzle, *Aerospace Science and Technology*. 71 (2017) 299-311. <https://doi.org/10.1016/j.ast.2017.09.001>.
- [14] H. Ling, R.C. Chou, S.W. Lee, Shooting and bouncing rays: calculating the RCS of an arbitrarily shaped cavity, *IEEE Transactions on Antennas and Propagation*. 37 (2) (1989) 194-205. <https://doi.org/10.1109/8.18706>.
- [15] N. Baranwal, S.P. Mahulikar, Aircraft engine's infrared lock-on range due to back pressure penalty from choked convergent nozzle, *Aerospace Science and Technology*, 39 (2014) 377-383. <https://doi.org/10.1016/j.ast.2014.09.020>.
- [16] N. Baranwal, S.P. Mahulikar, IR signature study of aircraft engine for variation in nozzle exit area, *Infrared Physics & Technology*. 74 (2016) 21-27. <https://doi.org/10.1016/j.infrared.2015.11.001>.
- [17] X.L. Sun, Z.X. Wang, L. Zhou, J.W. Shi, Z.W. Liu, Experimental and computational investigation of double serpentine nozzle, *Proceedings of the Institution of Mechanical Engineers, Part G: Journal of Aerospace Engineering*. 229 (11) (2015) 2035-2050. <https://doi.org/10.1177/0954410014564402>.
- [18] P. Sun, L. Zhou, Z.X. Wang, X.L. Sun, Effect of serpentine nozzle on bypass ratio of turbofan engine exhaust, *2018 Joint Propulsion Conference*. (2018) 4744. <https://doi.org/10.2514/6.2018-4744>.
- [19] E. Lindermeir, M. Rütten, IR-signature of the MULDICON configuration determined by the IR-signature model MIRA, *2018 Applied Aerodynamics Conference*. (2018) 3166. <https://doi.org/10.2514/6.2018-3166>.
- [20] Y. Shan, X. Zhou, X. Tan, J. Zhang, Y. Wu, Parametric design method and performance analysis of double s-shaped nozzles, *International Journal of Aerospace Engineering*. 2019. <https://doi.org/10.1155/2019/4694837>.
- [21] W. Cheng, Z. Wang, L. Zhou, J. Shi, X. Sun, Infrared signature of serpentine nozzle with engine swirl, *Aerospace Science and Technology*. 86 (2019) 794-804. <https://doi.org/10.1016/j.ast.2019.01.057>.
- [22] S.Y. Noh, J.Y. Bae, J.H. Kim, J.Y. Nam, H. Jo, H.H. Cho, Analysis of flow and infrared signature characteristics according to ucav nozzle shape, *Journal of the Korean Society of Propulsion Engineers*. 23 (5) (2019) 27-35. <https://doi.org/10.6108/KSPE.2019.23.5.027>.
- [23] Z. Hui, J. Shi, L. Zhou, Z. Wang, Y. Liu, Experimental investigation of serpentine nozzles for turbofan, *Aerospace Science and Technology*. 117 (2021) 106892. doi.org/10.1016/j.ast.2021.106892.
- [24] Y. Meng, J. Shi, L. Zhou, Z. Wang, Numerical investigation on flow characteristics of multi-stream supersonic nozzle with serpentine configuration, *Aerospace Science and Technology*. 144

- (2023) 108799. doi.org/10.1016/j.ast.2023.108799.
- [25] J. Paterson, Overview of low observable technology and its effects on combat aircraft survivability, *Journal of Aircraft*. 36 (2) (1999) 380-388. <https://doi.org/10.2514/2.2468>.
- [26] R. Whitford, Designing for stealth in fighter aircraft (stealth from the aircraft designer's viewpoint), *SAE Technical Paper*. (1996) 965540, <https://doi.org/10.4271/965540>.
- [27] G.W. Stimson, *Introduction to Airborne Radar*, Hughes Aircraft Company, El Segundo, CA, 1983, 126-128.
- [28] A.C. Brown, Fundamentals of low radar cross-sectional aircraft design, *Journal of Aircraft*. 30 (3) (1993). <https://doi.org/10.2514/3.46331>.
- [29] X. Guo, Q. Yang, H. Yang, K. Du, Radar cross section measurement of double S-shaped nozzle with radar absorbing material, *Selected Papers of the Chinese Society for Optical Engineering Conferences*. 10255 (2016) 924-931. <https://doi.org/10.1117/12.2267508>.
- [30] Z.Y. Zhou, J. Huang, Joint improvements of radar/infrared stealth for exhaust system of unmanned aircraft based on sorting factor Pareto solution, *Scientific Reports*. 11 (1) (2021). <https://doi.org/10.21203/rs.3.rs-135958/v1>.
- [31] Z. Zhou, J. Huang, Mixed design of radar/infrared stealth for advanced fighter intake and exhaust system, *Aerospace Science and Technology*. 110 (2021) 106490. doi.org/10.1016/j.ast.2021.106490.
- [32] Y. He, Q. Yang, Y. Shi, X. Gao, H. Yang, Multi-objective optimization design of S-shaped inlet with internal bump, *Aerospace Science and Technology*. 130 (2022) 107901. doi.org/10.1016/j.ast.2022.107901.
- [33] C.H. An, D.W. Kang, S.T. Baek, R.S. Myong, S.M. Kim, S.M. Choi, Analysis of plume infrared signatures of S-shaped nozzle configurations of aerial vehicle, *Journal of Aircraft*. 53 (6) (2016) 1768-1778. doi.org/10.2514/1.C033685.
- [34] M.J. Kang, S.H. Ryu, K.J. Jung, H. Lee, R.S. Myong, Shape optimization of single serpentine nozzle to minimize observability of UCAV, *Journal of the Korean Society for Aeronautical & Space Sciences*. 57 7 (2023) 477-486. <https://doi.org/10.5139/JKSAS.2023.51.7.1>.
- [35] Y.R. Lee, J.W. Lee, C.M. Shin, R.S. Myong, Characteristics of flow field and IR of double serpentine nozzle plume for varying cross sectional areas and flight conditions in UCAV, *Journal of the Korean Society for Aeronautical & Space Sciences*. 49 (8) (2021) 689-698. <https://doi.org/10.5139/JKSAS.2021.49.8.689>.
- [36] ANSYS FLUENT User's Manual 2021 R1, ANSYS, Canonsburg, PA 15317, 2021.
- [37] H.J. Lee, J.H. Lee, R.S. Myong, S.M. Kim, S.M. Choi and W.C. Kim, Computational and experimental investigation of thermal flow field of micro turbojet engine with various nozzle configurations, *Journal of The Korean Society for Aeronautical and Space Sciences*. 46 (2) (2018) 150-158. <https://doi.org/10.5139/JKSAS.2018.46.2.150>.
- [38] C.B. Ludwig, W. Malkmus, J.E. Reardon, J.A.L. Thomson, R. Goulard, Handbook of infrared

- radiation from combustion gases, *NASA-SP-3080* (1973).
- [39] Goody, R.M. and Yung, Y.L., *Atmospheric Radiation: Theoretical Basis*, Oxford University Press, 2nd ed., New York, 1989. <https://doi.org/10.1093/oso/9780195051346.001.0001>.
- [40] W.L. Grosshandler, RADCAL: a narrow-band model for radiation calculations in a combustion environment, *National Institute of Standards and Technology*, 1402 (1993). <http://archive.org/details/radcalnarrowband1402gros>.
- [41] J.H. Chae, J.H. Lee, J.W. Lee, N.K. Ha, D.G. Kim, H.S. Jang, R.S. Myong, Computational analysis of effects of thermal flow field and chemical components on their signature in the exhaust plume of a micro jet engine, *Journal of Computational Fluids Engineering*. 24 (3) (2019) 101-111. <https://doi.org/10.6112/ksce.2019.24.3.101>.
- [42] Y.R. Lee, J.W. Lee, C.M. Shin, J.W. Kim, R.S. Myong, Particle layer effects on flowfield and infrared characteristics of aircraft exhaust plume, *Journal of Aircraft*. 59 (5) (2022) 1320-1336. <https://doi.org/10.2514/1.C036744>.
- [43] W.J. Sun, Q.H. Gao, J.Z. Zhang, F. Hu, Y. Shan, Aerosol infrared stealth technology: theory and development of infrared suppression and particle dispersion in aircraft plume, *Thermal Science and Engineering Progress*. 39 (2023) 101695. <https://doi.org/10.1016/j.tsep.2023.101695>.
- [44] W.C. Chew, J.M. Jin, E. Michielssen, J. Song, *Fast and Efficient Algorithms in Computational Electromagnetics*, Artech House, Inc, Boston 2001.
- [45] *Altair FEKO User's Manual v2022*, Altair Engineering, United States, 2022.
- [46] A.K. Dominek, M.C. Gilreath, R.M. Wood, Almond test body, U.S. Patent No. 4,809,003, filed 28 Feb. 1989.
- [47] A.C. Woo, H.T.G. Wang, M.J. Schuh, M.L. Sanders, Benchmark radar targets for the validation of computational electromagnetics programs, *IEEE Antennas and Propagation Magazine*. 35 (1) (1993) 84-89. <https://doi.org/10.1109/74.210840>.
- [48] F. Obelleiro-Basteiro, J.L. Rodriguez, R.J. Burkholder, An iterative physical optics approach for analyzing the electromagnetic scattering by large open-ended cavities, *IEEE Transactions on Antennas and Propagation*. 43 (4) (1995) 356-361. <https://doi.org/10.1109/8.376032>.
- [49] J.S. Seybold, K.L. Weeks, Arithmetic versus geometric mean of target radar cross section, *Microwave and Optical Technology Letters*. 11 (5) (1996) 265-270. [https://doi.org/10.1002/\(sici\)1098-2760\(19960405\)11:5<265::aid-mop9>3.0.co;2-c](https://doi.org/10.1002/(sici)1098-2760(19960405)11:5<265::aid-mop9>3.0.co;2-c).